Palacky University
Faculty of Natural Sciences
Department of Optics

Tomographic methods in modern optics

Bohumil Stoklasa

A thesis presented for the degree of
Doctor of Philosophy

Olomouc 2014

Declaration

This is to certify that:

- I was collaborating on all numerical analysis in chapters 4,5,6.
- I have performed all experiments in chapter 4.
- The experimental part described in chapter 6 has been performed by Ch. Müller et al. in laboratories Max Planck Institute Erlangen. I was collaborating on the analysis of the experimental data.

Acknowledgements

First of all, I would like to thank my supervisor, Jaroslav Řeháček who introduced me the world of science and supported me during my phd studies.

I would like to thank Zdeněk Hradil for collaboration, inspiring discussions and support. Special thanks belongs to L.L.Sanchez-Soto for nice collaboration and my abroad stays in Madrid and Erlangen. Further, I would like to thank M. Baránek and Y.S. Teo, and other members of Department of Optics for various support.

Finally, my warmest thanks go to my family and Jana.

Thank you.

Contents

Chapter 1

Goals of the thesis

The aim of the Thesis is to present my work in the field of tomographic methods in the modern optics. Applications in the classical optics as well in the quantum optics are presented as solution of three topics, namely wavefront-detection tomography, photon distribution tomography and quantum-polarization state tomography. Here, quantum state tomography formalism provides general framework for all problems in the thesis. Brief contemporary state of research in this fields is described in chapter 2. Chapter 3 includes experimental and numerical tools for tomography measurements. Especially, experimental devices and detailed explanation of numerical tomography algorithms are discussed. Using these fundamentals the particular experiments and tomography protocols developed during the past five years are described in details.

Tomography of wavefront sensor which enables a measurement of coherence properties of light beam is a subject of chapter 4. First experimental realization of the method is described as a successful reconstruction of vortex beam coherence matrix, together with vortex beam 3D imaging experiments. Maximum likelihood iterative algorithm developed for a reconstruction of quantum state density matrix was used for a coherence matrix reconstruction, which determines coherence properties of light beam. In the second part of the chapter, wavefront tomography with informationally incomplete measurement is described as a successful demonstration of Maximul Likelihood-Maximum Entropy method. All experiments involved classical high intensity light and demonstrate application of quantum state tomography formalism to classical signals.

In chapter 5, application of data pattern tomography protocol is proposed. The method solve the problem of measurement apparatus calibration by measuring responses to know input probe states. The costly detector calibration is than bypassed by using a direct fitting of data in terms of detector responses. Problem of choosing proper probe states for particular measurement is discussed together with numerical verification of the protocol on photon number resolving detector.

In our contribution, the device is based on time-multiplexing principle.

Chapter 6 reports a tomographic reconstruction of the polarization sector of a bright polarization squeezed beam starting from a complete set of Stokes measurement. Given the symmetry that underlines the polarization structure of quantum fields, the unique Wigner distribution is used to represent states. Direct reconstruction of the distribution by an inverse Radon transform is compared with the results of a maximum likelihood estimation. A novel maximum likelihood algorithm experimentally proves to provide significantly higher statistical inversion stability than the standard inverse Radon transform.

The main results of the thesis are reviewed in chapter 7, where we also give brief outlook of future work. The list of my publications, citations index and bibliography are given at the end of the thesis.

The main chapters of this thesis containing new scientific results are based on the following papers:

B. Stoklasa, L. Motka, J. Rehacek, Z. Hradil, L. L. Sánchez-Soto, *Wavefront sensing reveals optical coherence,* Nature Communications **5**, (2014)

D. Mogilevtsev, A. Ignatenko, A. Maloshtan, B. Stoklasa, J. Rehacek, Z. Hradil, *Data pattern tomography: reconstruction with an unknown apparatus,* N. J. Phys. **14**, (2013)

CH. Müller, B. Stoklasa, A. B. Klimov, Ch. Gabriel, Ch. Peuntinger, J. Rehacek, Z. Hradil, L. L. Sanchez-Soto, Ch. Marquardt, G. Leuchs, *Quantum polarization tomography of bright squeezed light,* N. J. Phys. **14**, (2012)

Y. S. Teo, B. Stoklasa, B.G. Englert, J. Rehacek, Z. Hradil, *Incomplete quantum state estimation: a comprehensive study,* Phys. Rev. A. **85**, 042317 (2012)

Chapter 2

Contemporary state of research

Light is a major carrier of information about the universe around us, from the smallest to the largest scale. Measuring light properties may be a difficult task, especially in quantum optics. As a fundamental feature of quantum mechanics, we cannot see physical object in their full complexity, because of Heisenberg uncertainty principle. Tomography techniques were developed more than twenty years ago [1, 2] to overcome these fundamental limitations. Quantum states may comprise complementary features that cannot be measured simultaneously and precisely. However, no principal obstacle exists to observing all complementary aspects in a series of distinct experiments on identically prepared objects [3]. We can state the main challenge of quantum state tomography as follows: given a finite set of identical copies of a system in a state represented by the density matrix ρ, the state must be inferred from the measured relative frequencies f_l, which sample the true probabilities p_l of distinct measurement outcomes [4]. With these limited resources, the choice of optimal measurements and the design of efficient reconstruction algorithm turn to be decisive [5, 6].

In this thesis, three different properties of light are measured with the help of tomography concept, particularly coherence properties of light beams, photon number distribution of light pulses and polarization state of bright squeezed light. Quantum tomography is a general framework in all cases, that is why the first section of the chapter is dedicated to a survey of quantum tomography protocols. While the photon number distribution of light pulses measurement serves as a background for development of a special tomography protocol in the thesis, chapters dedicated to coherence properties of light beams and polarization properties of bright squeezed light present the experimental results. Hence, two sections of this chapter gives the overview of the experimental methods.

2.1 Quantum tomography protocols

Quantum state preparation is the first important step for any protocol that makes use of quantum resources. Examples of such protocols are quantum state teleportation and quantum key distribution which require entangled quantum states. In order to verify the integrity of the quantum state of the source prepared, one carries out *quantum state tomography* on the source. Measurements are performed on a collection of quantum systems (electrons, photons, etc.) that are emitted from the source, that is, a *quorum*. Then, the quantum state of the source is inferred from the measurement data obtained from this ensemble. The measurements are generically described by a set of positive operators Π_j that compose a *probability operator measurement* (POM). The procedure of state inference is also known as *quantum state estimation*. If the size of the ensemble is infinite, the estimation procedure will yield the unique *true* quantum state of the source; this is the frequentist's definition of the true state, which we accept as the best description of what the source prepares. However, such an ensemble is never achievable in any laboratory setting, as one can only perform measurements on a *finite* ensemble of quantum systems. As a result, the state estimator obtained will be different from the true state and depends on the details of the estimation procedure. To make statistical predictions, the corresponding operator $\hat{\rho}$ describing this estimator must be a *statistical operator*, which is positive. This will ensure that the estimated probability $\hat{p}_j = \mathrm{tr}\{\hat{\rho}\Pi_j\}$ for an outcome Π_j of *any* set of POM is positive. We shall denote all estimated quantities with a "hat" symbol.

There are two popular methods for quantum state estimation: *Bayesian* and *maximum-likelihood* (ML). The Bayesian state estimation method [7–9] constructs a state estimator from an integral average over all possible quantum states. The *likelihood functional*, which yields the likelihood of obtaining a particular sequence of measurement detection with a given quantum state, serves as a weight for the average. This approach includes all the neighboring states near the maximum of the likelihood functional as possible guesses for the unknown ρ_{true}. These neighboring states are given especially significant weight when N is small, in which case the likelihood functional is only broadly peaked at the maximum. However, the integral average unavoidably depends on how one measures volumes in the state space, and there is no universal and unambiguous method for that. The ML approach [4, 10–12], on the other hand, simply chooses the estimator as the statistical operator that maximizes the likelihood functional. Rather than identifying a unique estimator, as the Bayesian approach always does, the ML method may only yield a convex set of estimators if the estimated probabilities $\hat{p}_j$ are consistent with more than one statistical operator. If the ML estimator is unique, and the quorum sufficiently large, both approaches give the same estimator since the likelihood functional peaks very strongly at the maximum.

When the measurement outcomes form an *informationally complete* set, the measurement data obtained will contain maximal information about the source. Thus, a unique state estimator can be inferred with ML. Unfortunately, in tomography experiments performed on complex quantum systems with many degrees of freedom, it is not possible to implement such an informationally complete set of measurement outcomes. As a result, some information about the source will be missing and its quantum state cannot be completely characterized. The ML estimator obtained from these informationally incomplete data is no longer unique and there will in general be infinitely many other ML estimators which are consistent with the data. In Ref. [78], an iterative algorithm (MLME) to estimate unknown quantum states from incomplete measurement data by maximizing the likelihood and *von Neumann entropy* functionals is briefly reported. In that Letter, it is assumed that the measurement detections are perfect with no detection losses, i.e. $\sum_j \Pi_j = 1$. The application of this algorithm was illustrated with examples of homodyne tomography and it is concluded that, together with a more objective Hilbert space truncation, this approach can serve as a reliable and statistically meaningful quantum state estimation with incomplete data.

For successful reconstruction of quantum state several technical as well as mathematical pre-requisites are needed. A well calibrated detection device performing sufficiently accurate measurement of the signal is an indispensable part of any reconstruction protocol. However, the calibration is a formidable task by itself, especially if it is to be done with few-photon states. This problem has received increased attention recently, particularly, the so-called "absolute" calibration was developed, see [14–19]. Mathematically, the problem of characterizing an unknown measurement device is closely related to the dimensionality of the parameter space [20]. For a search subspace of the dimension N there are about N^2 parameters characterizing a density matrix and therefore N^4 elements of a rank-4 tensor are needed for the description of the link between an arbitrary input signal and measured outcome. A detailed discussion of detector tomography and related techniques can be found in [21]. High dimensions of the reconstruction spaces are often required for a faithful characterization of complex quantum systems [22]. Despite recent progress in the field of quantum process estimation [23, 24], the problem is far from being solved.

2.2 Shack-Hartmann tomography

Three-dimensional objects emit radiation that can be viewed as complex wavefronts shaped by diverse features, such as refractive index, density, or temperature of the emitter. These wavefronts are specified by both their amplitude and phase; yet, as conventional optical detectors measure only (time-averaged) intensity, in-

formation on the phase is discarded. This information turns out to be valuable for a variety of applications, such as optical testing [25], image recovery [26], displacement and position sensing [27], beam control and shaping [28–30], as well as active and adaptive control of optical systems [31], to mention but a few.

Actually, there exists a diversity of methods for wavefront reconstruction, each one with its own pros and cons [32]. Such methods can be roughly classified into three categories: (a) interferometric methods, based on the superposition of two beams with a well-defined relative phase; (b) methods based on the measurement of the wavefront slope or wavefront curvature, and (c) methods based on the acquisition of images followed by the application of an iterative phase-retrieval algorithm [33]. Notwithstanding the enormous progress that has already been made, practical and robust wavefront sensing still stands as an unresolved and demanding problem [34].

The time-honored example of the Shack-Hartmann (SH) wavefront sensor surely deserves a special mention [35]: its wide dynamical range, high optical efficiency, white light capability, and ability to use continuous or pulsed sources make of this setup an excellent solution in numerous applications. The operation of the SH sensor appeals to the intuition, giving the overall impression that the underlying theory is obvious [36]. Indeed, it is often understood in an oversimplified geometrical-optics framework, which is much the same as assuming full coherence of the detected signal. By any means, this is not a complete picture: even in the simplest instance of beam propagation, the coherence features turn out to be indispensable [37].

It has been recently suggested [38] that SH sensing can be reformulated in a concise quantum notation. This is more than an academic curiosity, because it immediately calls for the application of the methods of quantum state reconstruction [4]. Accordingly, one can verify right away that wavefront sensors may open the door to an assessment of the mutual coherence function, which conveys full information on the signal.

2.3 Quantum polarization tomography

Polarization of light is a robust characteristic that can be efficiently manipulated using modest equipment without introducing more than marginal losses. It is thus not surprising that this is often the variable of choice to encode quantum information, as one can convince oneself by looking at some recent cutting-edge experiments, including quantum key distribution [39], quantum dense coding [40], quantum teleportation [41], rotationally invariant states [42], phase super-resolution [43], and weak measurements [44].

In the discrete-variable regime of single, or few, photons, one is mostly inter-

ested into two-mode states, which for all practical purposes can be regarded as a spin system [45, 46]. As a result, the polarization state can be determined from correlation functions of different orders [47–57]. Given the small dimensionality of the Hilbert space involved, the state reconstruction can be readily performed.

In the continuous-variable case, polarization properties are exploited for an expedient generation, manipulation, and measurement of nonclassical light. Polarization squeezing [58–61], which has been observed in numerous experiments [62–66], is perhaps the most tantalizing illustration. Full Stokes polarimetry [67] is the method employed by the majority of the practitioners in this area.

However, the reconstruction in this limit is a touchy business and requires special care. The origin of the problem can be traced back to the fact that the characterization of the polarization state by the whole density operator is superfluous, because it contains much more than polarization information. This redundancy can easily be handled for low number of photons, but becomes a real hurdle for highly excited states. An adequate solution has been proposed recently: it suffices with a subset of the density matrix that has been called the "polarization sector" [68, 69] or the "polarization density operator" [70]. Its knowledge allows for a complete specification of the state on the Poincaré sphere (actually on a set of nested spheres that can be appropriately called the Poincaré space). The technique was devised by Karassiov and coworkers [71–73] and implemented experimentally in [74].

Chapter 3

Methods and tools

Different light properties measured by tomographical methods are discussed in the thesis, namely coherence function of classical light, polarization of bright squeezed light and photon distribution of light pulses. Each quantity requires unique measuring schemes and numerical methods for inverting measured data. Nevertheless, common framework of all problems is a formalism of quantum state tomography even in the case of classical coherence function, as will be explained. This formalism and numerical algorithms for quantum tomography are discussed in the first part of the chapter, description of three measuring schemes follows.

3.1 Formalism and numerical algorithms of quantum state estimation

In a tomography experiment, an ensemble of N copies of quantum systems, identically prepared, is measured using a POM which consists of positive measurement outcomes Π_j. For simplicity, we first assume that all measurement detections are perfect and hence $\sum_j \Pi_j = 1$. The problem of imperfect detections will be dealt with in Sec. 3.1.2. For each outcome, its number of occurrences is denoted by n_j such that $\sum_j n_j = N$. The likelihood functional $\mathscr{L}(\{n_j\};\rho)$, for a particular sequence of independent detections, is then

$$\mathscr{L}(\{n_j\};\rho) = \prod_j p_j^{n_j}\,. \tag{3.1}$$

As a consequence of perfect measurement detections, $\sum_j p_j = 1$. The ML procedure searches for the estimator $\hat{\rho}_{\mathrm{ML}}$ which maximizes $\mathscr{L}(\{n_j\};\rho)$. For a D-dimensional Hilbert space, when a POM comprises D^2 or more measurement outcomes, of which D^2 of them are linearly independent, it is informationally complete. In this case, there exists a unique estimator $\hat{\rho}_{\mathrm{ML}}$ for a given set of

measurement data $\{n_j\}$. One can also define the outcome frequencies $f_j = n_j/N$ out of these measurement data such that $\sum_j f_j = 1$. The corresponding functional $\mathscr{L}(\{n_j\};\rho)$ due to this informationally complete POM will peak at the unique global maximum $\hat{\rho}_{\rm ML}$ over the space of ρ, whereby $\hat{\rho}_{\rm ML}$ is solely determined by the frequencies f_j and does not depend on the total number N of measured copies.

The situation is different when the POM is informationally incomplete. In this case, there will be infinitely many ML estimators satisfying a smaller set of linearly independent constraints imposed by the incomplete measurement data. These ML estimators form a convex set of operators which maximize the convex functional $\mathscr{L}(\{n_j\};\rho)$. Geometrically, $\mathscr{L}(\{n_j\};\rho)$ possesses a convex plateau structure hovering over the space of ρ. The task, now, is to select one of these estimators for future statistical predictions. To do this, we adopt the well-known maximum-entropy (ME) principle advocated by Jaynes [75]. That is, we look for the estimator with the largest von Neumann entropy

$$S(\rho) = -\mathrm{tr}\{\rho \log \rho\} \tag{3.2}$$

among the convex set of ML estimators. This supplementary step introduces a small and smooth convex hill over the plateau structure so that a unique maximum can be obtained. The corresponding MLME estimator $\hat{\rho}_{\rm MLME}$ is the least-bias estimator for the given set of incomplete measurement data; it can be regarded as the most conservative guess of the unknown quantum state out of the convex set of ML estimators.

At this point, we would like to comment on the distinction between this MLME technique and the conventional ME technique [76, 77]. The ME technique takes the outcome frequencies f_j as *bona fide* estimates for the probabilities p_j and tries to search for the positive operator

$$\hat{\rho}_{\rm ME} = \frac{\mathrm{e}^{\sum_j \lambda_j \Pi_j}}{\mathrm{tr}\Big\{\mathrm{e}^{\sum_j \lambda_j \Pi_j}\Big\}} \tag{3.3}$$

that maximizes $S(\rho)$, subjected to the probability constraints which are mediated by the Lagrange multipliers λ_j. The fundamental problem with this scheme is that the f_js cannot always be treated as probabilities since there may not be *any* statistical operator ρ for which $f_j = \mathrm{tr}\big\{\rho\Pi_j\big\}$. This is due to the statistical noise which is inherent in the outcome frequencies arising from measuring a finite ensemble of quantum systems. Therefore, in such cases, the ME technique fails as there simply is no positive operator which is consistent with the measurement data to begin with. The MLME algorithm, on the other hand, looks for the unique MLME estimator by confining the search within the plateau region inside the space of statistical operators. Thus, positivity is ensured. In cases where the f_js are probabil-

ities, both the ME and MLME schemes yield the same estimator by construction since the estimated probabilities $\hat{p}_j = f_j$ correspond to a statistical operator.

3.1.1 Perfect measurements

Assuming that the measurement detections are perfect, the likelihood functional $\mathscr{L}(\{n_j\};\rho)$ in Eq. (3.1) gives a complete statistical description of all possible sequences of detections for the N measured copies of quantum systems. Equivalently, one can consider the optimization of the *normalized log-likelihood functional* $\log(\mathscr{L}(\{n_j\};\rho))/N$ to simplify the subsequent calculations, in view of the monotonic nature of the logarithmic function. The motivation for introducing the normalization will become clear soon. The MLME scheme can then be perceived as a standard constrained optimization problem: maximize $\log(\mathscr{L}(\{n_j\};\rho))/N$ subjected to the constraint that $S(\rho)$ takes the maximal value $S_{\max}$. This is equivalent to maximizing $S(\rho)$ with the constraint that $\log(\mathscr{L}(\{n_j\};\rho))/N$ is maximal, as discussed above. The Lagrange functional for this optimization problem is defined as

$$\mathscr{I}(\lambda;\rho) = \lambda\left(S(\rho) - S_{\max}\right) + \frac{1}{N}\log\mathscr{L}(\{n_j\};\rho)\,, \tag{3.4}$$

where λ is the Lagrange multiplier corresponding to the constraint for $S(\rho)$. We denote the estimator that maximizes $\mathscr{I}(\lambda;\rho)$ by $\hat{\rho}_{\mathrm{I},\lambda}$. Incidently, the functional $\mathscr{I}(\lambda;\rho)$ is a sum of two different types of entropy, up to an irrelevant additive constant $\sum_j f_j \log f_j$: the von Neumann entropy $S(\rho)$ that quantifies the "lack of information", and the *negative* of the *relative entropy* $S(\{f_j\}|\{p_j\}) = \sum_j f_j \log(f_j/p_j)$ that quantifies the "gain of information" from the measurement data. The scheme can now be interpreted as a simultaneous optimization of two complementary aspects of information, with an appropriately assigned constant relative weight λ. In addition, the normalization of $\log\mathscr{L}(\{n_j\};\rho)$ renders the optimal value of λ to be independent of N.

When $\lambda = 0$, we recover the Lagrange functional for the log-likelihood functional alone. Owing to the informational incompleteness of the measurement data, there exists a convex plateau structure for the log-likelihood functional. As $\lambda \to \infty$, the von Neumann entropy becomes increasingly more significant and the resulting estimator $\hat{\rho}_{\mathrm{I},\lambda\to\infty}$ approaches the maximally-mixed state $1/D$. Naturally, when λ takes on a very small positive value, the contribution from $\lambda S(\rho)$ becomes much smaller than $\log(\mathscr{L}(\{n_j\};\rho))/N$ and the effect of the von Neumann entropy functional is only significant over the plateau region in which the likelihood is maximal. Figure 3.1 illustrates all the aforementioned points.

This means that, in general, λ should be chosen so small that $S\left(\hat{\rho}_{\mathrm{I},\lambda}\right)$ is very close to the minimum, and below which there are only very slight changes in the two entropy functionals [78].

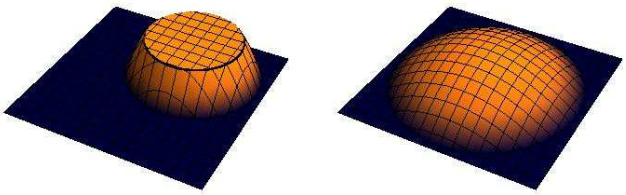

(a) $\lambda = 0$ (b) $\lambda \to \infty$

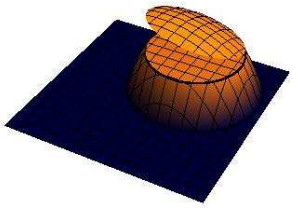

(c) $\lambda = 10^{-3}$

Figure 3.1: Schematic diagrams of $\mathscr{I}(\lambda, \rho)$ on the space of statistical operators. The maximally-mixed state resides at the center of the square base which represents the Hilbert space. At the extremal points of λ, $\mathscr{I}(\lambda = 0; \rho) = \log(\mathscr{L}(\{n_j\}; \rho))/N$, with a convex plateau at the maximal value, and $\mathscr{I}(\lambda \to \infty; \rho) = \lambda S(\rho)$. Plot (c) shows the functional with an appropriate choice of value for λ for MLME. An additional hill-like structure resulting from $S(\rho)$ is introduced over the plateau, so that the estimator with the largest entropy can be selected from the convex set of ML estimators within the plateau.

Let us derive the iterative algorithm for maximizing $\mathscr{I}(\lambda \to 0; \rho)$ with respect to ρ. After varying $\mathscr{I}(\lambda \to 0; \rho)$, we have

$$\delta \mathscr{I}(\lambda \to 0; \rho) = -\lambda \operatorname{tr}\{\delta\rho \log \rho\} + \sum_j \frac{f_j}{p_j} \delta p_j \,. \tag{3.5}$$

The variations δp_j, or $\delta\rho$, have to be such that ρ stays positive after these variations. To choose their appropriate forms, we first parameterize the positive operator $\rho = \mathscr{A}^\dagger \mathscr{A} / \operatorname{tr}\{\mathscr{A}^\dagger \mathscr{A}\}$ with an auxiliary complex operator $\mathscr{A}$. Under this parametrization,

$$\delta\rho = \frac{\delta\mathscr{A}^\dagger \mathscr{A} + \mathscr{A}^\dagger \delta\mathscr{A} - \rho \operatorname{tr}\{\delta\mathscr{A}^\dagger \mathscr{A} + \mathscr{A}^\dagger \delta\mathscr{A}\}}{\operatorname{tr}\{\mathscr{A}^\dagger \mathscr{A}\}} \,. \tag{3.6}$$

Substituting $\delta\rho$ in Eq. (3.6) into Eq. (3.5), we have

$$\delta\mathscr{I}(\lambda\to 0;\rho)=\mathrm{tr}\left\{\frac{\delta\mathscr{A}^\dagger\mathscr{A}}{\mathrm{tr}\{\mathscr{A}^\dagger\mathscr{A}\}}\mathfrak{R}+\mathfrak{R}\frac{\mathscr{A}^\dagger\delta\mathscr{A}}{\mathrm{tr}\{\mathscr{A}^\dagger\mathscr{A}\}}\right\}, \tag{3.7}$$

where

$$\mathfrak{R}=R-1-\lambda\left(\log\rho-\mathrm{tr}\{\rho\log\rho\}\right) \tag{3.8}$$

with

$$R=\sum_j\frac{f_j}{p_j}\Pi_j\,. \tag{3.9}$$

When $\mathscr{I}(\lambda\to 0;\rho)$ is maximal, we have $\delta\mathscr{I}(\lambda\to 0;\rho)=0$ and the extremal equations

$$\rho\,\mathfrak{R}=\mathfrak{R}\rho=0 \tag{3.10}$$

are satisfied. Therefore, to solve these extremal equations numerically, we iterate the equation

$$\rho_{\mathrm{k+1}}=\frac{\left(\mathscr{A}_k^\dagger+\delta\mathscr{A}_k^\dagger\right)\left(\mathscr{A}_k+\delta\mathscr{A}_k\right)}{\mathrm{tr}\left\{\left(\mathscr{A}_k^\dagger+\delta\mathscr{A}_k^\dagger\right)\left(\mathscr{A}_k+\delta\mathscr{A}_k\right)\right\}} \tag{3.11}$$

starting from some statistical operator ρ_1, until $k=k'$ such that the norm of $\rho_{k'}\mathfrak{R}_{k'}$ is less than some pre-chosen value. We then take $\hat{\rho}_{\mathrm{MLME}}\equiv\rho_{k'}$ as the MLME estimator. Maximizing $\mathscr{I}(\lambda\to 0;\rho)$ will require $\delta\mathscr{I}(\lambda\to 0;\rho)$ to be positive whenever $\mathscr{I}(\lambda\to 0;\rho)$ is less than the maximal value. A straightforward way to enforce positivity is to set

$$\delta\mathscr{A}_k\equiv\left(\delta\mathscr{A}_k^\dagger\right)^\dagger\equiv\varepsilon\mathscr{A}_k\mathfrak{R}_k\propto\varepsilon\frac{\partial\mathscr{I}(\lambda;\rho)}{\partial\mathscr{A}_k}\,, \tag{3.12}$$

with ε being a small positive constant. This is the *steepest-ascent* method. We have thus established a numerical MLME scheme as a set of iterative equations (3.11) and (3.12) to search for the MLME estimator using the measurement data obtained from perfect measurement detections. More compactly, the relevant iterative equations are

$$\begin{aligned}\rho_{\mathrm{k+1}}&=\frac{(1+\varepsilon\mathfrak{R}_k)\,\rho_k\,(1+\varepsilon\mathfrak{R}_k)}{\mathrm{tr}\{(1+\varepsilon\mathfrak{R}_k)\,\rho_k\,(1+\varepsilon\mathfrak{R}_k)\}}\,,\\ \mathfrak{R}_k&=R_k-1-\lambda\left(\log\rho_k-\mathrm{tr}\{\rho_k\log\rho_k\}\right).\end{aligned} \tag{3.13}$$

We note that a more efficient algorithm, using the conjugate-gradient method, can be derived from this steepest-ascent algorithm, which is the subject of a separate discussion.

3.1.2 Imperfect measurements

In actual experiments, the measurement detections will usually be imperfect in the sense that the detection efficiency η_j of a particular measurement outcome Π_j is less than unity. In this case, the overall outcome probabilities

$$\tilde{p}_j \equiv \eta_j p_j \tag{3.14}$$

will not sum to unity. Hence, we have a set of POM with outcomes $\tilde{\Pi}_j \equiv \eta_j \Pi_j$ such that $G \equiv \sum_j \tilde{\Pi}_j < 1$. A consequence of this is that the true total number M of copies received is not known, since only $N < M$ are detected ($N = M$ when all $\eta_j = 1$ as in Sec. 3.1.1).

The likelihood functional that accounts for all M copies of quantum systems in an experiment with imperfect detections is given by

$$\tilde{\mathscr{L}}(\{n_j\};\rho) = \frac{M!}{N!\,(M-N)!} \left(\prod_j \tilde{p}_j^{n_j} \right) (1-\eta)^{M-N}\,, \tag{3.15}$$

where $\eta = \sum_j \tilde{p}_j < 1$. The additional combinatorial prefactor arises from the indistinguishability in the ordering of the detection sequence resulted from losses. With the help of Stirling's approximation for the factorials, the variation of the corresponding log-likelihood functional is given by

$$\begin{aligned} \delta \log \tilde{\mathscr{L}}(\{n_j\};\rho) = \mathrm{tr}\left\{ \left(N\tilde{R} - \frac{M-N}{1-\eta} G \right) \delta\rho \right\} \\ + \delta M \log \left(\frac{(1-\eta)M}{M-N} \right), \end{aligned}$$

where $\tilde{R} = \sum_j f_j \tilde{\Pi}_j / \tilde{p}_j$. Adopting the concept of maximum-likelihood, we derive an expression for M such that $\log \tilde{\mathscr{L}}(\{n_j\};\rho)$ is maximized for any given ρ. This implies that the coefficient of the arbitrary δM must vanish and we have $M = N/\eta$ as the most-likely value of M. With this, the expression for $\tilde{\mathscr{L}}(\{n_j\};\rho)$ reduces to the simple form

$$\tilde{\mathscr{L}}(\{n_j\};\rho) = \prod_j \left(\frac{p_j}{\eta} \right)^{n_j} \tag{3.16}$$

up to an irrelevant multiplicative factor, with its corresponding logarithmic variation

$$\delta \log \tilde{\mathscr{L}}(\{n_j\};\rho) = N \mathrm{tr}\left\{ \left(\tilde{R} - \frac{G}{\eta} \right) \delta\rho \right\}. \tag{3.17}$$

The additional term $-\delta\rho G/\eta$ in the argument of the trace accounts for copies that have escaped detection.

Defining $\mathscr{I}(\lambda \to 0; \rho)$ for the new POM and its $\tilde{\mathscr{L}}(\{n_j\}; \rho)$ in Eq. (3.16), one can derive the iterative equations

$$\rho_{k+1} = \frac{\left(1+\varepsilon\tilde{\mathfrak{R}}_k\right)\rho_k\left(1+\varepsilon\tilde{\mathfrak{R}}_k\right)}{\mathrm{tr}\left\{\left(1+\varepsilon\tilde{\mathfrak{R}}_k\right)\rho_k\left(1+\varepsilon\tilde{\mathfrak{R}}_k\right)\right\}},$$
$$\tilde{\mathfrak{R}}_k = \tilde{R}_k - \frac{G}{\eta^{(k)}} - \lambda\left(\log\rho_k - \mathrm{tr}\{\rho_k \log\rho_k\}\right), \tag{3.18}$$

with $\eta^{(k)} = \sum_j \tilde{p}_j^{(k)}$.

To highlight the importance of a proper treatment of imperfect measurement detections, we perform a simulation on 10^3 randomly generated qubit states. Figure 3.2 compares the performance of the MLME algorithm derived in Sec. 3.1.1, with which we search for the MLME estimator by assuming that the measured data $\{n_j\}$ are all we have while ignoring the possible missing data, with that of the MLME algorithm derived in this section. The trace-class distance

$$\mathscr{D}_{\mathrm{tr}} = \frac{1}{2}\mathrm{tr}\{|\hat{\rho}_{\mathrm{MLME}} - \rho_{\mathrm{true}}|\} \tag{3.19}$$

is used as the figure of merit to quantify the distance between $\hat{\rho}_{\mathrm{MLME}}$ and ρ_{true}. The lesson here is that if one neglects the consequence of imperfect measurements in performing state reconstruction, the quality of the resulting reconstructed state estimator will typically be much lower than that obtained from a scheme which accounts for this imperfection.

3.1.3 Pattern tomography

The idea beyond the quantum state reconstruction using data patterns [79] bears obvious similarity to the image processing [143]. The density matrix, ρ, of the signal state is supposed to be represented as a mixture

$$\rho = \sum_{j=1}^{N} x_j \sigma_j, \tag{3.20}$$

where the coefficients x_j are real scalars (not necessarily positive) and σ_j are density matrices describing a set of linearly independent (generally, nonorthogonal) probe states.

A measurement described by a positive-valued operator measure (POVM), Π_l, is done on a set of probe states, σ_j. Obtained data represents data patterns used for fitting the data measured for an unknown state to be reconstructed. Consequently, due to the linearity, unknown signal state can be expanded (represented)

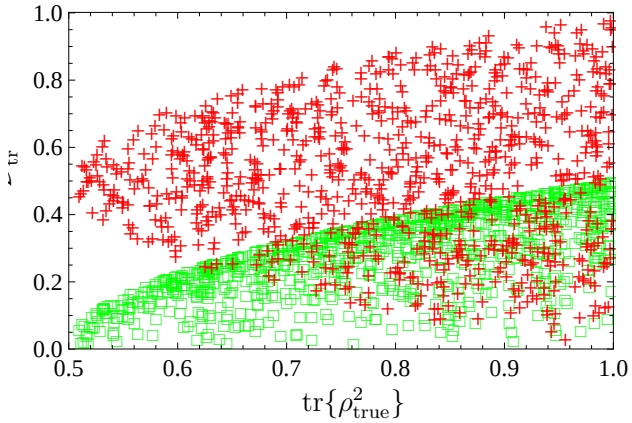

Figure 3.2: A comparison of two different schemes with 10^3 random qubit true states distributed uniformly with respect to the Hilbert-Schmidt measure. Fifty experiments were simulated for every true state, with $N = 5000$ for each experiment, and the respective average trace-class distances $\mathscr{D}_{\rm tr}^{\rm avg}$ were computed. The entire simulation was done with a set of randomly generated, informationally incomplete POM consisting of two imperfect measurement outcomes. The plot markers denoted by "+" represent reconstructed states using the algorithm in Eq. (3.13) while ignoring the imperfection of the measurements, and those denoted by "□" represent the reconstructed states using the algorithm in Eq. (3.18) that accounts for this imperfection. The significant improvement in tomographic efficiency with the latter algorithm is a strong indication of the importance of a proper treatment of imperfect measurements.

as a mixture of probe states with the same set of coefficients. Responses of the measurement set-up to the probe states are described by the matrix of probabilities

$$\bar{P}_{lj} = Tr\{\Pi_l \sigma_j\}. \tag{3.21}$$

The result of a practical estimation with a finite number of copies is a matrix of frequencies – the data pattern matrix P_{lj}. Now, the response f_l to an unknown signal can be expanded in the responses to probe states

$$f_l = \sum_j x_j P_{lj} \tag{3.22}$$

and the coefficients x_j can be estimated. Those coefficients are then used in the superposition Eq. (5.1) to yield the estimated state ρ. The quantumness of such a process is manifested by the positivity constraint imposed on the fitting procedure: The fitting of Eq. (3.22) must yield a set of x_j making the reconstruction ρ obtained from Eq. (5.1) positive semi-definite. Practical feasibility of this scheme

was demonstrated in Ref. [79]. An essential feature of the fitting procedure is that one does not need any knowledge about the POVM elements. The knowledge required for the reconstruction is obtained in the process of building the data pattern matrix. It is not necessary to perform a complete tomography of the measurement set-up, since only the probe states contributing significantly to the representation of a particular signal state are needed. The data pattern procedure can be reformulated as the process of updating information about the measurement set-up until a sufficiently accurate fit is obtained.

3.2 SH tomography

This section introduces an alternative theory for wavefront detection, based on the principles of quantum state tomography. We confine ourselves to the example of the Shack-Hartmann (SH) wavefront sensor. The operation of wavefront sensor is most often understood in an oversimplified geometrical-optics framework, which is much the same as assuming full coherence of the signal. Unfortunately, this naive picture breaks down when the light is partially coherent, because the very notion of a single wavefront becomes somewhat ambiguous: the signal has to be conceived as a statistical mixture of many wavefronts [134]. To circumvent this difficulty, we observe that these sensors provide a simultaneous detection of position and angular spectrum (i.e., directions) of the incident radiation. In other words, the SH is a pertinent example of a simultaneous unsharp position and momentum measurement, a question of fundamental importance in quantum theory and about which much has been discussed [82–84]. We will point out that common wavefront sensors can be utilized for measuring mutual coherence and hence 3D imaging of partially coherent fields provided quantum state reconstruction techniques are adopted for data processing.

3.2.1 SH wavefront sensing

The working principle of the SH wavefront sensor can be elaborated with reference to Fig. 3.3. An incoming light field is divided into a number of sub-apertures by a microlens array that creates focal spots, registered in a CCD camera. The deviation of the spot pattern from a reference measurement allows the local direction angles to be derived, which in turn enables the reconstruction of the wavefront. In addition, the intensity distribution within the detector plane can be obtained by integration and interpolation between the foci.

Rephrasing the SH operation in a quantum parlance will prove pivotal for the remaining discussion. Let ρ be the coherence matrix of the field to be analyzed. Using an obvious Dirac notation, we can write $G(\mathbf{x}',\mathbf{x}'') = \langle \mathbf{x}'|\rho|\mathbf{x}''\rangle =$

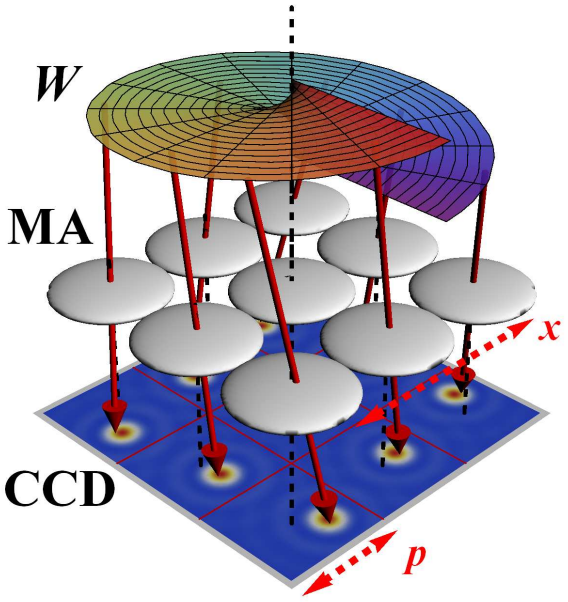

Figure 3.3: **The principle of the SH wavefront sensor.** A microlens array (MA) subdivides the wavefront (W) into multiple beams that are focused in a CCD camera. Local slope of the wavefront over each microlens aperture determines the location of the spot on the CCD. Red arrows represent normals to the wavefront.

$\mathrm{Tr}(\rho|\mathbf{x}'\rangle\langle\mathbf{x}''|)$, where $|\mathbf{x}\rangle$ is a vector describing a point-like source located at $\mathbf{x}$ and Tr is the matrix trace. Thereby, the mutual coherence function $G(\mathbf{x}',\mathbf{x}'')$ appears as the position representation of the coherence matrix. As a special case, the intensity distribution across a transversal plane becomes $I(\mathbf{x}) = \mathrm{Tr}(\rho|\mathbf{x}\rangle\langle\mathbf{x}|)$. Moreover, a coherent beam of complex amplitude $U(\mathbf{x})$, can be assigned to a ket $|U\rangle$, such that $U(\mathbf{x}) = \langle\mathbf{x}|U\rangle$.

To simplify, we restrict the discussion to one dimension, denoted by x. If the setup is illuminated with a coherent signal $U(x)$, and the ith microlens is Δx_i apart from the SH axis, this microlens feels the field $U(x-\Delta x_i) = \langle x|\exp(-i\Delta x_i P)|U\rangle$, where P is the momentum operator. This field is truncated and filtered by the aperture (or pupil) function $A(x) = \langle x|A\rangle$ and Fourier transformed by the microlens prior to being detected by the CCD camera. All this can be accounted for in the form

$$U'(\Delta p_j) = \langle A|\exp(-i\Delta p_j X)\exp(-i\Delta x_i P)|U\rangle\,, \tag{3.23}$$

where X is the position operator and we have assumed that the jth pixel is an-

gularly displaced from the axis by Δp_j. The intensity measured at the jth pixel behind the ith lens is then governed by a Born-like rule

$$I(\Delta x_i, \Delta p_j) = \mathrm{Tr}(\rho |\pi_{ij}\rangle\langle\pi_{ij}|)\,, \tag{3.24}$$

with $|\pi_{ij}\rangle = \exp(i\Delta x_i P)\exp(i\Delta p_j X)|A\rangle$. As a result, each pixel performs a projection on the position- and momentum-displaced aperture state.

Some special cases of those aperture states are particularly appealing. For pointlike microlenses, $A(x) \to \delta(x)$ and $|\pi_{ij}\rangle \to |x = \Delta x_i\rangle$ (i.e., a position eigenstate): they produce broad diffraction patterns and information about the transversal momentum is lost. Conversely, for very large microlenses, $A(x) \to 1$ and $|\pi_{ij}\rangle \to |p = \Delta p_j\rangle$ (i.e., a momentum eigenstate): they provide a sharp momentum measurement with the corresponding loss of position sensitivity. A most interesting situation is when one uses a Gaussian approximation [38]; now $A(x) = \exp(-x^2/2)$, which implies $|\pi_{ij}\rangle \to |\alpha_{ij}\rangle$, that is, a coherent state of amplitude $\alpha_{ij} = \Delta x_i + i\Delta p_j$. This means that the measurement in this case projects the signal on a set of coherent states and hence yields a direct sampling of the Husimi distribution [85] $Q(\alpha) = \langle\alpha|\rho|\alpha\rangle$.

This quantum analogy provides quite a convenient description of the signal: different choices of CCD pixels and/or microlenses can be interpreted as particular phase-space operations [86].

3.2.2 SH tomography

Unlike the Gaussian profiles discussed before, in a realistic setup the microlens apertures do not overlap. If we introduce the operators $\Pi_{ij} = |\pi_{ij}\rangle\langle\pi_{ij}|$, the measurements describing two pixels belonging to distinct apertures are compatible whenever $[\Pi_{ij}, \Pi_{i'j}] = 0$, $i \neq i'$, which renders the scheme informationally incomplete [87]. Signal components passing through distinct apertures are never recombined and the mutual coherence of those components cannot be determined.

Put differently, the method cannot discriminate signals comprised of sharply-localized non-overlapping components. Nevertheless, these problematic modes do not set any practical restriction. As a matter of fact, spatially bounded modes (i.e., with vanishing amplitude outside a finite area) have unbounded Fourier spectrum and so, an unlimited range of transversal momenta. Such modes cannot thus be prepared with finite resources and they must be excluded from our considerations: for all practical purposes, the SH performs an informationally complete measurement and any practically realizable signal can be characterized with the present approach.

To proceed further in this matter, we expand the signal as a finite superposition of a suitable spatially-unbounded computational basis (depending on the

actual experiment, one should use plane waves, Laguerre-Gauss beams, etc). If that basis is labeled by $|k\rangle$ ($k = 1, \ldots, d$, with d being the dimension), the complex amplitudes are $\langle x|k\rangle = \psi_k(x)$. Therefore, the coherence matrix ρ and the measurement operators Π_{ij} are given by $d \times d$ non-negative matrices. A convenient representation of Π_{ij} can be obtained directly from Eq. (3.24), viz,

$$\left(\Pi_{ij}\right)_{mn} = \psi_{n,i}(\Delta p_j)\, \psi^*_{m,i}(\Delta p_j), \tag{3.25}$$

where $\psi_{m,i}(x)$ is the complex amplitude at the CCD plane of the ith lens generated by the incident mth basis mode ψ_m.

This idea can be illustrated with the simple yet relevant example of square microlenses: $A(x) = \mathrm{rect}(x)$. We decompose the signal in a discrete set of plane waves $\psi_k(x) = \exp(-ip_k x)$, parametrized by the transverse momenta p_k. This is just the Fraunhofer diffraction on a slit, and the measurement matrix is

$$\left(\Pi_{ij}\right)_{mn} = \mathrm{sinc}(\Delta p_j + p_m)\mathrm{sinc}(\Delta p_j + p_n) e^{i(p_m - p_n)\Delta x_i}. \tag{3.26}$$

The smallest possible search space consists of two plane waves (which is equivalent to a single-qubit tomography). By considering different pixels j belonging to the same aperture i, linear combinations of only three out of the four Pauli matrices can be generated from Eq. (3.26). For example, a lens placed on the SH axis ($\Delta x_i = 0$) fails to generate σ_y and at least one more lens with a different Δx_i needs to be added to the setup to make the tomography complete.

This argument can be easily extended: the larger the search space, the more microlenses must be used. In this example, the maximum number of independent measurements generated by the SH detection is $(2M+1)d - 3M$, for M lenses. A d-dimensional signal —a spatial qudit— can be characterized with about $M \sim d/2$ microlenses. This should be compared to the d quadratures required for the homodyne reconstruction of a photonic qudit [88, 89].

3.3 Polarization sqeezed light tomography

In this section we present a comprehensive treatment of polarization tomography. As with any reliable quantum tomographical scheme, we need to supply three key ingredients [90]: the availability of a tomographically complete measurement, a suitable representation of the quantum states, and a robust algorithm for inverting the experimental data. In this respect, we use a standard Stokes scheme that implements the first ingredient in a very simple way; for the second, we resort to the well-known SU(2) Wigner distribution [91–98], and finally, we prove that the inversion of the data in terms of that Wigner function is an inverse three-dimensional (3D) Radon transform.

3.3.1 Polarization structure of quantum fields

A satisfactory description of the polarization structure of quantum fields and the corresponding observables that specify this structure is of paramount importance for our purposes.

We restrict our attention to the case of a monochromatic plane wave (the formalism can be easily extended to more involved multimode wavefronts [100, 101]), which we assume to propagate in the z direction, so its electric field lies in the xy plane. Under these conditions, we are dealing with a two-mode field that can be fully characterized by two complex amplitude operators. They are denoted by $\hat{a}_H$ and $\hat{a}_V$, where the subscripts H and V indicate horizontally and vertically polarized modes, respectively. The commutation relations of these operators are

$$[\hat{a}_k, \hat{a}_\ell^\dagger] = \delta_{k\ell}\,, \qquad k,\ell \in \{H,V\}\,. \tag{3.27}$$

The description is greatly simplified if we use the Schwinger representation [102, 103]

$$\hat{J}_1 = \tfrac{1}{2}(\hat{a}_H^\dagger \hat{a}_V + \hat{a}_V^\dagger \hat{a}_H)\,, \qquad \hat{J}_2 = \tfrac{i}{2}(\hat{a}_H \hat{a}_V^\dagger - \hat{a}_H^\dagger \hat{a}_V)\,, \qquad \hat{J}_3 = \tfrac{1}{2}(\hat{a}_H^\dagger \hat{a}_H - \hat{a}_V^\dagger \hat{a}_V)\,, \tag{3.28}$$

together with the total number

$$\hat{N} = \hat{a}_H^\dagger \hat{a}_H + \hat{a}_V^\dagger \hat{a}_V\,. \tag{3.29}$$

These operators coincide, up to a factor 1/2, with the Stokes operators [104], whose average values are precisely the classical Stokes parameters [105]. Using equation (3.27), one immediately notices that $\hat{\mathbf{J}} = (\hat{J}_1, \hat{J}_2, \hat{J}_3)$ satisfy the commutation relations of the su(2) algebra

$$[\hat{J}_k, \hat{J}_\ell] = i\varepsilon_{k\ell m}\hat{J}_m\,, \tag{3.30}$$

where $\varepsilon_{k\ell m}$ is the Levi-Civita fully antisymmetric tensor. This noncommutability precludes the simultaneous exact measurement of the physical quantities they represent. Among other consequences, this implies that no field state (apart from the vacuum) can have sharp nonfluctuating values of all the operators $\hat{\mathbf{J}}$ simultaneously. This is expressed by the uncertainty relation

$$\Delta^2 \hat{\mathbf{J}} = \Delta^2 \hat{J}_1 + \Delta^2 \hat{J}_2 + \Delta^2 \hat{J}_3 \geq \langle \hat{N} \rangle / 2\,, \tag{3.31}$$

where the variances are given by $\Delta^2 \hat{J}_i = \langle \hat{J}_i^2 \rangle - \langle \hat{J}_i \rangle^2$. In other words, the electric vector of a monochromatic quantum field never traces out a definite ellipse.

In classical optics, the total intensity is a well-defined quantity and the Poincaré sphere appears thus as a smooth surface with radius equal to that intensity. In quantum optics we have

$$\hat{J}_1^2 + \hat{J}_2^2 + \hat{J}_3^2 = \left(\frac{\hat{N}}{2}\right)\left(\frac{\hat{N}}{2} + \mathbb{1}\right)\,, \tag{3.32}$$

and, as fluctuations in the number of photons are unavoidable (leaving aside photon-number states), we are forced to talk of a three-dimensional Poincaré space (with axis J_1, J_2 and J_3) that can be envisioned as foliated in a set of nested spheres with radii proportional to the different photon numbers that contribute significantly to the state.

The Hilbert space $\mathscr{H}$ of these two-mode fields has a convenient orthonormal basis in the form of Fock states for both polarization modes, namely $|n_H, n_V\rangle$. However, since

$$[\hat{N}, \hat{\mathbf{J}}] = 0\,, \tag{3.33}$$

each subspace with a fixed number of photons N must be handled separately. In other words, in the previous onion-like picture of the Poincaré space, each shell has to be addressed independently. This can be emphasized if instead of the Fock basis, we employ the relabeling

$$|J, m\rangle \equiv |n_H = J + m, n_V = J - m\rangle\,, \tag{3.34}$$

According to (3.32), we have that $J = N/2$ and this basis can be also seen as the common eigenstates of $\{\hat{J}^2, \hat{J}_3\}$. In this way, for each fixed J (i.e., fixed number of photons N), m runs from $-J$ to J and these states span a $(2J+1)$-dimensional subspace wherein $\hat{\mathbf{J}}$ acts in the usual way (in units $\hbar = 1$)

$$\begin{aligned} \hat{J}_\pm |J, m\rangle &= \sqrt{J(J+1) - m(m \pm 1)}\, |J, m \pm 1\rangle\,, \\ \hat{J}_3 |J, m\rangle &= m |J, m\rangle\,, \end{aligned} \tag{3.35}$$

with $\hat{J}_\pm = \hat{J}_1 \pm \hat{J}_2$.

It is clear from all this previous discussion that the moments of any energy-preserving observable (such as $\hat{\mathbf{J}}$) do not depend on the coherences between different subspaces. The only accessible information from any state described by the density matrix $\hat{\rho}$ is thus its polarization sector, which is specified by the block-diagonal form

$$\hat{\rho}_{\text{pol}} = \bigoplus_J \hat{\rho}^{(J)} \tag{3.36}$$

where $\hat{\rho}^{(J)}$ is the reduced density matrix in the J subspace. Any $\hat{\rho}$ and its associated block-diagonal form $\hat{\rho}_{\text{pol}}$ cannot be distinguished in polarization measurements (and, accordingly, we drop henceforth the subscript pol). This is consistent with the fact that polarization and intensity are, in principle, independent concepts: in classical optics the form of the ellipse described by the electric field (polarization) does not depend on its size (intensity).

3.3.2 Polarization squeezing and the dark plane

The variances of the angular-momentum operators (3.28) are not independent, for they are constrained by

$$\Delta^2\hat{J}_k\,\Delta^2\hat{J}_\ell \geq \varepsilon_{k\ell m}\,|\langle\hat{J}_m\rangle|^2\,. \tag{3.37}$$

It is always possible to find pairs of maximally conjugate operators for this uncertainty relation. This is equivalent to establishing a basis in which only one of the operators (3.28) has a nonzero expectation value, say $\langle\hat{J}_k\rangle = \langle\hat{J}_\ell\rangle = 0$ and $\langle\hat{J}_m\rangle \neq 0$. The only nontrivial Heisenberg inequality reads thus

$$\Delta^2\hat{J}_k\,\Delta^2\hat{J}_\ell \geq |\langle\hat{J}_m\rangle|^2\,. \tag{3.38}$$

Polarization squeezing can then be sensibly defined as [58–61]:

$$\Delta^2\hat{J}_k < |\langle\hat{J}_m\rangle| < \Delta^2\hat{J}_\ell\,. \tag{3.39}$$

The choice of the conjugate operators $\{\hat{J}_k,\hat{J}_\ell\}$ is by not means unique: there exists an infinite set $\{\hat{J}_\perp(\theta),\hat{J}_\perp(\theta+\pi/2)\}$ that are perpendicular to the state classical excitation $\hat{J}_m$, for which $\langle\hat{J}_\perp(\theta)\rangle = 0$ for all θ. All these pairs exist in the J_k–J_ℓ plane, which is called the "dark plane" because it is the plane of zero mean intensity. We can express a generic $\hat{J}_\perp(\theta)$ as $\hat{J}_\perp(\theta) = \hat{J}_k\cos\theta + \hat{J}_\ell\sin\theta$, θ being an angle defined relative to $\hat{J}_k$. Condition (3.39) is then equivalent to

$$\Delta^2\hat{J}_\perp(\theta_{\rm sq}) < \tfrac{1}{2}|\langle\hat{N}\rangle| < \Delta^2\hat{J}_\perp(\theta_{\rm sq}+\pi/2), \tag{3.40}$$

where $\hat{J}_\perp(\theta_{\rm sq})$ is the squeezed parameter and $\hat{J}_\perp(\theta_{\rm sq}+\pi/2)$ the antisqueezed parameter.

In the experiments presented in this paper, a focal role will be played by the example in which the horizontal and vertical modes have the same amplitude but are phase shifted by $\pi/2$: $\langle\hat{a}_H\rangle = i\langle\hat{a}_V\rangle = i\alpha/\sqrt{2}$, α being a real number. This light is circularly polarized and fulfills $\langle\hat{J}_1\rangle = \langle\hat{J}_3\rangle = 0$, $\langle\hat{J}_2\rangle = \alpha^2$. It is advantageous to work in the circular polarization basis, whose right $(+)$ and left $(-)$ amplitudes are given in terms of the linear ones by

$$\hat{a}_\pm = \frac{1}{\sqrt{2}}(\hat{a}_H \pm i\,\hat{a}_V)\,. \tag{3.41}$$

In this manner, $\langle\hat{a}_+\rangle = \alpha$ and $\langle\hat{a}_-\rangle = 0$. The operators in the J_1–J_3 plane correspond to the quadrature operators of the dark left-polarized mode. In fact, expressing the fluctuations of $\hat{\mathbf{J}}$ in terms of the noise of the circularly polarized modes $\delta\hat{a}_\pm$ and assuming $|\langle\delta\hat{a}_\pm\rangle| \ll \alpha$ we find [106]

$$\delta\hat{J}_\perp(\theta) = \alpha\delta\hat{X}_-(\theta) = \alpha[\delta\hat{X}_H(\theta) + \delta\hat{X}_V(\theta+\pi/2)]\,, \tag{3.42}$$

where $\hat{X}_i = (\hat{a}_i e^{-i\theta} + \hat{a}_i^\dagger e^{i\theta})/\sqrt{2}$ are the rotated quadratures for the ith amplitude. On the other hand, we have that

$$\delta\hat{N} = \alpha(\delta\hat{a}_+ + \delta\hat{a}_+^\dagger) = \alpha\,\delta\hat{X}_+\,, \tag{3.43}$$

and the intensity exhibits no dependence on the dark mode. In consequence, the condition (3.40) can be recast for this example as

$$\Delta^2\hat{J}_\perp(\theta) < |\langle\alpha\rangle|^2 \quad \Leftrightarrow \quad \Delta^2\hat{X}_-(\theta) < 1\,, \tag{3.44}$$

that is, polarization squeezing is equivalent to vacuum squeezing in the orthogonal polarization mode.

In the dark-plane measurements, the beam is divided equally between two photodetectors. Such measurements are then identical to balanced homodyne detection: the classical excitation is a local oscillator for the orthogonally polarized dark mode. The phase between these modes is varied by rotating the measurement through the dark plane, allowing a full characterization of the noise properties. This is a unique feature of polarization measurements and has been used in many experiments [107–111].

3.3.3 Polarization Wigner function

The structure discussed so far highlights that SU(2) is the symmetry group for polarization. To provide an appropriate phase-space description of states, we take advantage of the pioneering work of Stratonovich [91] and Berezin [92], who introduced quasi-probability distribution functions on the sphere satisfying all the proper requirements. This construction was later generalized by others [93–98] and has proved to be very useful in visualizing properties of spinlike systems [112–116]

To gain physical insights into this approach, let us start by representing the density matrix with respect to the polarization basis. Instead of using directly the states $\{|J,m\rangle\}$, it is more convenient to write such an expansion as

$$\hat{\rho}^{(J)} = \sum_{K=0}^{2J}\sum_{q=-K}^{K} \rho_{Kq}^{(J)}\,\hat{T}_{Kq}^{(J)}\,, \tag{3.45}$$

where the irreducible tensor operators $T_{Kq}^{(J)}$ are [117]

$$\hat{T}_{Kq}^{(J)} = \sqrt{\frac{2K+1}{2J+1}} \sum_{m,m'=-J}^{J} C_{Jm,Kq}^{Jm'}\,|J,m'\rangle\langle J,m|\,, \tag{3.46}$$

with $C^{Jm'}_{Jm,Kq}$ being the Clebsch-Gordan coefficients that couple a spin J and a spin K ($0 \leq K \leq 2J$) to a total spin J. These tensor operators have the right transformation properties under rotations and they indeed constitute the most suitable orthonormal basis

$$\mathrm{Tr}[\hat{T}^{(J)}_{Kq}\,\hat{T}^{(J')\,\dagger}_{K'q'}] = \delta_{JJ'}\delta_{KK'}\delta_{qq'}\,. \tag{3.47}$$

Although at first sight they might look a little bit intimidating, they are nothing but the multipoles used in atomic physics [118]: one can check that

$$\hat{T}^{(J)}_{00} = \frac{1}{\sqrt{2J+1}}\hat{\mathbb{1}} \qquad \hat{T}^{(J)}_{1q} = \sqrt{\frac{3}{(2J+1)(J+1)J}}\hat{J}_q \quad q=\pm,z\,, \tag{3.48}$$

and similarly the $\hat{T}^{(J)}_{Kq}$ can be related to the Kth power of the generators (3.28). Accordingly, the expansion coefficients

$$\rho^{(J)}_{Kq} = \mathrm{Tr}[\hat{\rho}^{(J)}\,T^{(J)\,\dagger}_{Kq}] \tag{3.49}$$

are known as state multipoles.

The Wigner function associated with the state (3.45) is

$$W^{(J)}(\theta,\phi) = \mathrm{Tr}[\hat{\rho}^{(J)}\,\hat{\Delta}^{(J)}(\theta,\phi)]\,, \tag{3.50}$$

where $\hat{\Delta}^{(J)}(\theta,\phi)$ is the Wigner kernel

$$\hat{\Delta}^{(J)}(\theta,\phi) = \sqrt{\frac{4\pi}{2J+1}}\sum_{K=0}^{2J}\sum_{q=-K}^{K} Y^*_{Kq}(\theta,\phi)\,\hat{T}^{(J)}_{Kq}\,, \tag{3.51}$$

and $Y_{Kq}(\theta,\phi)$ are the spherical harmonics. This kernel is unitary and satisfies the normalization conditions

$$\mathrm{Tr}[\hat{\Delta}^{(j)}(\theta,\phi)] = 1\,, \qquad \frac{2J+1}{4\pi}\int_{\mathscr{S}^2} d\Omega\;\hat{\Delta}^{(j)}(\theta,\phi) = \hat{\mathbb{1}}\,. \tag{3.52}$$

The integral extends over the unit sphere $\mathscr{S}^2$ and $d\Omega$ is the invariant measure therein, namely, $d\Omega = \sin\theta\, d\theta d\phi$.

From (3.50) and the properties of the irreducible tensors, one can immediately express the Wigner function in the very suggestive form

$$W^{(J)}(\theta,\phi) = \sum_{K=0}^{2J}\sum_{q=-K}^{K}\rho^{(J)}_{Kq}\,Y^*_{Kq}(\theta,\phi)\,, \tag{3.53}$$

which clearly shows that determining this Wigner function is tantamount to the knowledge of all the state multipoles. (i.e., all the moments of the Stokes parameters).

One can obtain the marginal of $W^{(J)}(\theta,\phi)$ once summed over all the values of J

$$W(\theta,\phi)=\sum_J \frac{2J+1}{4\pi} W^{(J)}(\vartheta,\varphi)\,, \tag{3.54}$$

where the factor has been introduced to ensure the proper normalization.

In the above-mentioned example of a strong circularly polarized state, we can consider that the sphere can locally be replaced by its tangent plane since $J \simeq \alpha^2$. Using simple geometrical relations between the coordinates (θ,ϕ) and the Cartesian coordinates (q,p) in that tangent plane, we get

$$W(\theta,\phi) \simeq \alpha\, W(q,p)\,, \tag{3.55}$$

which confirms that the dark plane is equivalent to the standard phase space for continuous variables.

In the limit of large photon numbers the representation (3.50) is not very useful. In such a case, a remarkably effective approximation is given by [119]

$$\hat{\Delta}^{(J)}(\theta,\phi) \simeq (-1)^J \exp(-i\pi \mathbf{n}\cdot\hat{\mathbf{J}})\,,$$

where $\mathbf{n}=(\cos\theta\sin\phi,\sin\theta\sin\phi,\cos\theta)$ is the unitary vector in the direction (θ,ϕ).

3.3.4 Tomograms and tomographic inversion

A general polarimetric apparatus consists of a half-wave plate, with axis at angle α, followed by a quarter-wave plate at angle β. For fixed values of the angles (α,β) of the wave plates, the selected direction in the Stokes space is

$$\theta=\pi/2-2\beta\,, \qquad \phi=2\beta-4\alpha\,. \tag{3.56}$$

The polarization transformations performed by the wave plates can be represented by $\hat{J}_2$, which generates rotations about the direction of propagation, and $\hat{J}_3$, which generates phase shifts between the modes. Their joint action is given by the operator

$$\hat{D}(\theta,\phi)=e^{i\theta\hat{J}_2}\,e^{i\phi\hat{J}_3}\,, \tag{3.57}$$

which describes displacements over the sphere. After that, a polarizing beam splitter projects onto the basis $|J,m\rangle$.

In physical terms, the wave plates transform the input polarization allowing the measurement of different Stokes parameters by the projection onto the basis $|J,m\rangle$. This can be modeled by

$$\hat{\Pi}_m^{(J)}=|J,m\rangle\langle J,m|\,, \tag{3.58}$$

so that $w_m^{(J)} = \mathrm{Tr}[\hat{\rho}\hat{\Pi}_m^{(J)}]$ is the probability of detecting $n_H = J+m$ photons in the horizontal mode and simultaneously $n_V = J-m$ photons in the vertical one. Of course, when the total number of photons is not measured and only the difference m is observed, it reduces to

$$\Pi_m = \sum_{J=|m|}^{\infty} |J,m\rangle\langle J,m| \,. \tag{3.59}$$

The experimental histograms recorded for each direction (θ,ϕ) correspond to the tomographic probabilities

$$w_m^{(J)}(\theta,\phi) = \mathrm{Tr}[\hat{\rho}\,\hat{\Pi}_m^{(J)}(\theta,\phi)] = \mathrm{Tr}[\hat{\rho}\,\hat{D}(\theta,\phi)\,\hat{\Pi}_m^{(J)}\,\hat{D}^{\dagger}(\theta,\phi)] \,. \tag{3.60}$$

The reconstruction in each $(2J+1)$-dimensional invariant subspace can now be carried out exactly since it is essentially equivalent to a spin J [120–123]. One can proceed in a variety of ways, but perhaps the simplest one is to look for an integral representation of the tomograms (3.60); as soon as one realizes that

$$\hat{\Pi}_m^{(J)}(\theta,\phi) = \frac{1}{2\pi}\int_0^{2\pi} d\omega \, \exp[i\omega(\hat{\mathbf{J}}\cdot\mathbf{n} - m)] \,, \tag{3.61}$$

the tomograms read as

$$w_m^{(J)}(\theta,\phi) = \frac{1}{2\pi}\int_0^{2\pi} d\omega \, \mathrm{Tr}[\hat{\rho}^{(J)} \exp(i\omega\hat{\mathbf{J}}\cdot\mathbf{n})]\, e^{-i\omega m} \,, \tag{3.62}$$

that is, they appear as the Fourier transform of the characteristic function for the observable $\hat{\mathbf{J}}\cdot\mathbf{n}$. After some direct manipulations, we find that

$$\hat{\rho}^{(J)} = \frac{1}{4\pi}\sum_{m=-J}^{J}\int_{\mathscr{S}_2} d\mathbf{n}' \, w_m^{(J)}(\mathbf{n}')\,\mathscr{K}(\hat{\mathbf{J}}\cdot\mathbf{n}' - m) \,, \tag{3.63}$$

where $d\mathbf{n}'$ indicates integration over the unit sphere and the kernel $\mathscr{K}(x)$ is

$$\mathscr{K}(x) = \frac{2J+1}{4\pi^2}\int_0^{2\pi} d\omega \, \sin^2\left(\frac{\omega}{2}\right) e^{-i\omega x} \,. \tag{3.64}$$

Although (3.63) is a formal solution, it is handier to map this density matrix onto the corresponding Wigner function, for which we need to compute $\mathrm{Tr}[\mathscr{K}(\mathbf{J}\cdot\mathbf{n}' - m)\,\hat{\Delta}^{(J)}(\theta,\phi)]$. When J is large enough, we can replace the Wigner kernel by its approximate expression (3.56), getting

$$\mathrm{Tr}[\mathscr{K}(\mathbf{J}\cdot\mathbf{n}' - m)\,\hat{\Delta}^{(J)}(\theta,\phi)] = (-1)^J \frac{2J+1}{4\pi^2}\int_0^{2\pi} d\omega \, \sin^2\left(\frac{\omega}{2}\right) e^{-im\omega}\chi_J(\omega') \,, \tag{3.65}$$

where $\chi_J(\omega')$ is the character of the $(2J+1)$-dimensional representation of the SU(2) group [117] and ω' is given by

$$\cos\left(\frac{\omega'}{2}\right) = \mathbf{n}\cdot\mathbf{n}'\sin\left(\frac{\omega}{2}\right). \tag{3.66}$$

For $J \gg 1$, m can be taken as a continuous variable. Replacing the sum by an integral, integrating by parts and taking into account that for localized states $\mathbf{n}\cdot\mathbf{n}' \simeq 1$, the Wigner function simplifies to

$$W(J,\theta,\phi) = \frac{2J+1}{4\pi^2}\int_{-\infty}^{\infty} dm \int_{\mathscr{S}_2} d\mathbf{n}' \frac{d^2 w_m^{(J)}(\mathbf{n})}{dm^2}\,\delta(m - J\,\mathbf{n}\cdot\mathbf{n}'), \tag{3.67}$$

where we have included J as an argument to stress that it must be treated as continuous. The reconstruction in this limit turns out to be equivalent to an inverse Radon transform of the measured tomograms.

3.4 Time-multiplexed detection tomography

Time-multiplexed detection (TMD) tomography [124] is a useful device for photon number distribution measurement. For experiments of this type, photon pulses, of a particular quantum state, containing more than one photon are sent through a series of beam splitters, each associated with a certain transmission probability. The word "beam splitter", used in this context, represents a class of possible apparatuses for splitting photon pulses, which includes conventional beam splitters, optical fibers, etc. Behind each of the output ports of such a series is a single-photon detector that either registers a click from an incoming split photon pulse, with some detection efficiency, or does nothing. Thus, each output port has a certain overall efficiency $\tilde{\eta}_j$ which is related to the relevant transmission probabilities and detection efficiency (See Fig. 3.4). As a consequence of this, the POM outcomes

$$\Pi_j = \sum_n |n\rangle c_{jn} \langle n| \tag{3.68}$$

will be a mixture of Fock states, with the coefficients c_{jn} related to η_j [125]. If there are N_{ports} output ports, where *all* η_js are different, there will be $2^{N_{\text{ports}}}$ distinct POM outcomes due to the binary nature of the single-photon detectors. In addition, $\sum_{j=1}^{2^{N_{\text{ports}}}} \Pi_j = 1$ since the $2^{N_{\text{ports}}}$ binary sequences of detection configurations constitute all possible events. These POM outcomes commute and a measurement of these outcomes only gives information about the diagonal entries of the statistical operator of the true state in the Fock basis. In order to obtain information about the off-diagonal entries, one can, for instance, displace the current set of

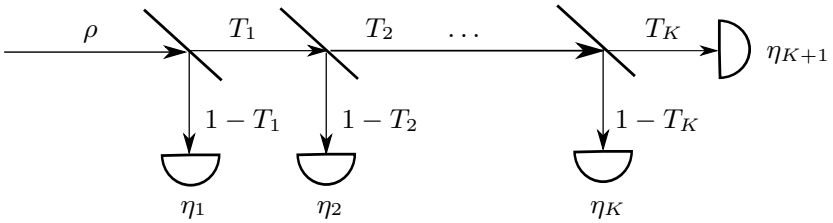

Figure 3.4: A schematic diagram representing the time-multiplexed setup with $K+1$ output ports. The T_js are the respective transmission probabilities for the jth beam splitter. The overall efficiency for, say, the kth port is given by $\tilde{\eta}_k = \eta_k(1-T_k+T_{K+1}\delta_{k,K+1})\prod_{j=1}^{k-1}T_j$.

$2^{N_{\text{ports}}}$ POM outcomes in phase space with some complex value α_k away from the origin using the displacement operator

$$\mathscr{D}(\alpha_k) = \mathrm{e}^{\alpha_k A^\dagger - \alpha_k^* A}, \tag{3.69}$$

where A is the standard photon annihilation operator. Then, the new set of outcomes

$$\Pi_j(\alpha_k) = \frac{1}{\mathscr{N}}\mathscr{D}(\alpha_k)\Pi_j\mathscr{D}^\dagger(\alpha_k), \tag{3.70}$$

with $\mathscr{N}$ being the total number of such displaced set of $2^{N_{\text{ports}}}$ outcomes, do not commute with the undisplaced set. These displaced outcomes are suitable for a measurement that is designed to obtain information about the unknown true state by sampling over multiple α_ks. Experimentally, these displaced POM outcomes can be realized with unbalanced homodyne detection [126].

Chapter 4

Wavefront sensing reveals optical coherence

Wavefront sensing is a set of techniques providing efficient means to ascertain the shape of an optical wavefront or its deviation from an ideal reference. Due to its wide dynamical range and high optical efficiency, the Shack-Hartmann (SH) is nowadays the most widely used of these sensors. In sec.3.2, we show that it actually performs a simultaneous measurement of position and angular spectrum of the incident radiation and, therefore, when combined with tomographic techniques previously developed for quantum information processing, the Shack-Hartmann can be instrumental in reconstructing the complete coherence properties of the signal. We confirm these predictions with an experimental characterization of partially coherent vortex beams, a case that cannot be treated with the standard tools. This seems to indicate that classical methods employed hitherto do not fully exploit the potential of the registered data.

In this chapter, we report the first experimental measurement of the coherence properties of an optical beam with a SH sensor. To that end, we have prepared several coherent and incoherent superpositions of vortex beams. Our strategy can efficiently disclose that information, whereas the common SH operation fails in the task. We start with the experimental setup description which is common for all experiments presented in the chapter. After successful demonstration of coherence matrix reconstruction, we illustrate the utility of the SH tomography with an experimental demonstration of 3D imaging (or digital propagation) of partially coherent fields. Last section of the chapter is dedicated to applications of the MLME (sec. 3.1) algorithm to wavefront tomography.

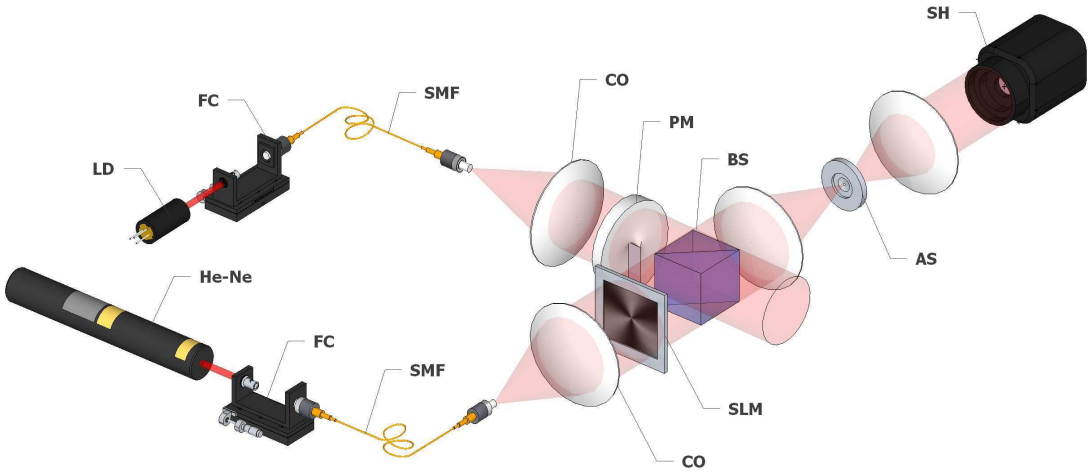

Figure 4.1: **Experimental layout for preparing and detecting partially coherent vortex beams.** Two independent laser sources, He-Ne at 633 nm (He-Ne) and a laser diode at 635 nm (LD), are coupled into single-mode fibers (SMF) by fiber couplers (FC). After collimation (CO) , they are transformed into vortex beams by two different techniques. The first beam, representing a coherent superposition of two vortex modes, is prepared by a digital hologram imprinted in a spatial light modulator (SLM). Unwanted diffraction orders are filtered by an aperture stop (AS), placed in a $4f$ system. The second beam is modulated by a vortex phase mask (PM) and represents a single vortex mode with opposite phase respect to the first beam. Both beams are incoherently mixed in a beam splitter (BS) and finally detected in a SH sensor (SH).

4.1 Partially-coherent beam preparation and detection.

Two independent vortex beams were created in the setup of Fig. 4.1 with two laser sources of nearly the same wavelength: a He-Ne (633 nm) and a diode laser (635 nm). The output beams were spatially filtered by coupling them into single-mode fibers. The power ratio between the modes was controlled by changing the coupling efficiency. The resulting modes were transformed into vortex beams by different methods.

The state $|V_{-3} - \frac{i}{2}V_{-6}\rangle$ was realized using a digital hologram prepared with an amplitude spatial light modulator (OPTO SLM), with a resolution of 1024×768 pixels. The hologram was then illuminated by a reference plane wave produced by placing the output of a single-mode fiber at the focal plane of a collimating lens. The diffraction spectrum involves several orders, of which only one contains useful information. To filter out the unwanted orders, a $4f$ optical processor, with

a 0.3 mm circular aperture stop placed at the rear focal plane of the second lens, was used. The resulting coherent vortex beam is then realized at the focal plane of the third lens. The second beam $|V_3\rangle$ was obtained trough a plane-wave phase profile modulation by a special vortex phase mask (RPC Photonics). Finally, the field in Eq. (5) was prepared by mixing the two vortex modes in a beam splitter.

During the state preparation, special care was taken to reduce any deviation between the true and target states. This involved minimizing aberrations as well as imperfections of the spatial light modulator, resulting in distortions of the transmitted wavefront.

The SH measurement involved a Flexible Optical array of 128 microlenses arranged in a hexagonal pattern. Each microlens has a focal length of 17.9 mm and a hexagonal aperture of 0.3 mm. The signal at the focal plane of the array is detected by a uEye CCD camera with a resolution of 640×480 pixels, each pixel being 9.9 μm×9.9 μm in size. Because of microlens array imperfections, CCD-microlens misalignment, and aberrations of the $4f$ processor (aberrations of the collimating optics are negligible), calibration of the detector must be carried out. The holographic part of the setup provided this calibration wave. SH data from the calibration wave and the partially coherent beam are shown in Fig. 4.2. The beam axis position in the microlens array coordinates was adjusted with a Gaussian mode. The detection noise is mainly due to the background light, which is filtered out prior to reconstruction.

4.2 Experimental SH tomography of partially-coherent vortex beams

We have validated our method with vortex beams [127, 128]. Consider the one-parameter family of modes specified by the orbital angular momentum ℓ, $V_\ell = \langle r,\varphi|\mathrm{V}_\ell\rangle \propto \mathrm{e}^{\mathrm{i}\ell\varphi}$, where (r,φ) are cylindrical coordinates. In our experiment, the partially coherent signal

$$\rho_{\text{true}} = |V_{-3} - \tfrac{i}{2}V_{-6}\rangle\langle V_{-3} - \tfrac{i}{2}V_{-6}| + \tfrac{1}{2}|V_3\rangle\langle V_3| \tag{4.1}$$

was created; that is, modes V_{-3} and V_{-6} are coherently superposed, while V_3 is incoherently mixed. Figure 4.1 sketches the experimental layout used to generate (4.1).

The reconstruction was done in the 7-dimensional space spanned by the V_ℓ modes with $\ell \in \{-9,-6,-3,0,+3,+6,+9\}$. The resulting matrix elements are plotted in Fig. 4.3. All in all, 49 real parameters had to be reconstructed. The data come from CCD areas belonging to 7 microlenses around the beam axis; each one of them comprise 11×11 pixels, which means 847 data samples altogether. An iterative maximum-likelihood algorithm [129, 130] (details in sec.3.1), was applied

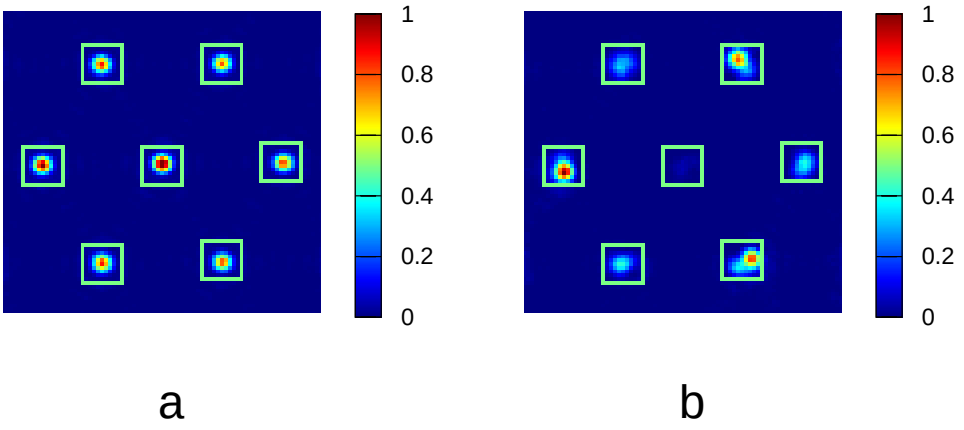

Figure 4.2: **Experimental CCD signal.** Rescaled 8-bit data corresponding to 7 microlenses placed in a hexagonal geometry, 81×81-pixels region, is displayed in both panels. a) Data of the plane wave used for calibration; b) data of the partially coherent vortex beam in Eq. (5). Green squares enclose the data used for the reconstruction. The intensity from the central microlens vanishes due to the presence of a phase singularity.

to estimate the true coherence matrix of the signal, whose results are summarized in Fig. 4.3. The main features of ρ_{true} are nicely displayed, which is also confirmed by the high fidelity of the reconstructed state $F(\rho_{\text{true}}, \rho) = \text{Tr}[\sqrt{\sqrt{\rho}\rho_{\text{true}}\sqrt{\rho}}] = 0.98$. The off-diagonal elements detect the coherence between modes, whereas the diagonal ones give the amplitude ratios between them. The reconstruction errors are mainly due to the difference between the true and the actually generated state.

To our best knowledge, this is the first experimental measurement of the coherence properties with a wavefront sensor. The procedure outperforms the standard SH operation, both in terms of dynamical range and resolution, even for fully coherent beams. For example, the high-order vortex beams with strongly helical wavefronts are very difficult to analyze with the standard wavefront sensors, while they pose no difficulty for our proposed approach.

The errors of the SH tomography can be quantified by evaluating the covariances of the parameters of the reconstructed coherence matrix ρ. In the absence of systematic errors, the Cramér-Rao lower bound [131, 132] can be employed to that end. In practice, a simpler approach based on the singular spectrum analysis [133] works pretty well. Let us decompose the $d \times d$ coherence matrix ρ (d is just the dimension of the search space) and the measurement operators Π_{ij} in an

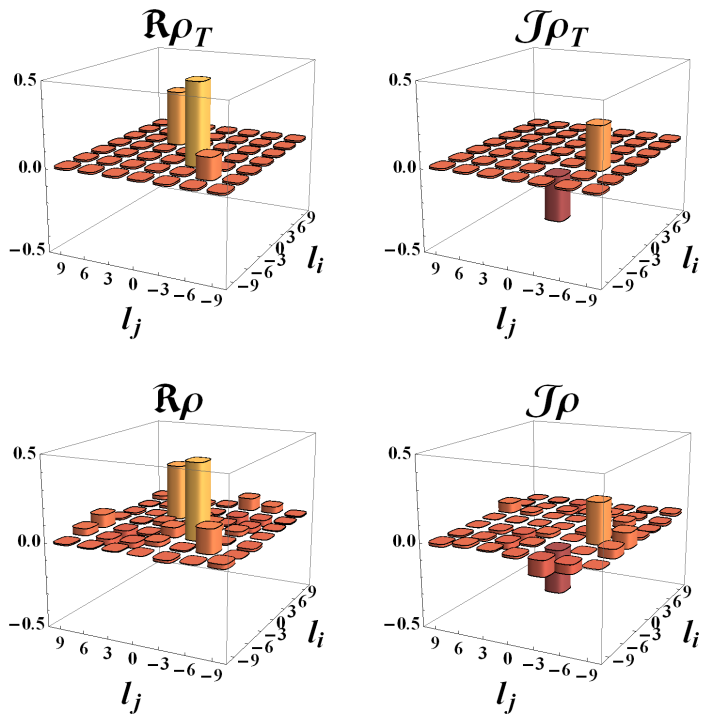

Figure 4.3: **Vortex-beam coherence-matrix reconstruction.** Real $\Re$ and imaginary $\Im$ parts of the coherence matrix for the true state ρ_{true} (upper panel) and for the reconstructed ρ (lower panel). The reconstruction space is spanned by vortex modes with $\ell \in \{-9,-6,-3,0,+3,+6,+9\}$. The nonzero values of $\Im\rho_{-6,-3}$ and $\Im\rho_{-3,-6}$ describe coherences between the modes $|V_{-6}\rangle$ and $|V_{-3}\rangle$ and the phase shift π between them. The very small values of $\rho_{3,-6}$, $\rho_{3,-3}$, $\rho_{-6,3}$ and $\rho_{-3,3}$ comes from the incoherent mixing of $|V_3\rangle$ and $|V_{-3} - \frac{i}{2}V_{-6}\rangle$. The fidelity of the reconstructed coherence matrix is $F = 0.98$.

orthonormal matrix basis Γ_k ($k = 1,\ldots,d^2$) [$\mathrm{Tr}(\Gamma_k\Gamma_l) = \delta_{kl}$], namely

$$\rho = \sum r_k\Gamma_k, \qquad \Pi_{ij} = \sum_k p_k^{ij}\Gamma_k, \tag{4.2}$$

so that the Born rule (3.24) can be recast as a system of linear equations

$$I_{ij} = \sum_k p_k^{ij} r_k\,. \tag{4.3}$$

Upon using a single index α to label all possible microlens/CCD-pixel combinations $\alpha \equiv \{i,j\}$, Eq. (4.3) can be concisely expressed in the matrix form

$$\mathbf{I} = \mathbf{P}\mathbf{r}\,, \tag{4.4}$$

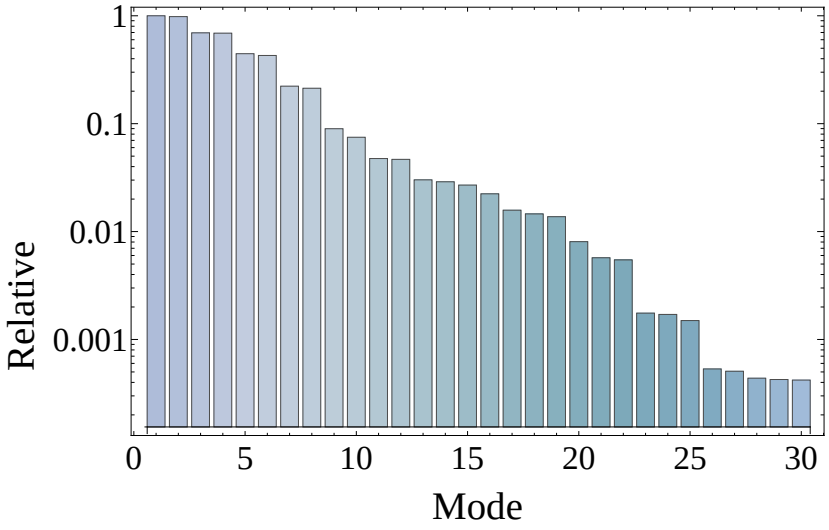

Figure 4.4: **Dynamical range of the SH reconstruction.** The singular spectrum $\{S_{kk}\}$ of the data in Fig. 4 (here, sorted and normalized to the largest singular value) quantifies the sensitivity of the tomography setup to the normal modes of the problem (see Methods). The relative strengths of the singular values correspond to the relative measuring accuracy of those modes. The dynamical range (or field of view) can be defined as the set of normal modes with singular values exceeding a given threshold.

where $\mathbf{I}$ is the vector of measured data, $\mathbf{r}$ is the vector of coherence-matrix parameters and $\mathrm{P}_{\alpha k} = p_k^\alpha$ is the tomography matrix.

Obviously, for ill-conditioned measurements, the reconstruction errors will be larger and *vice versa*. By applying a singular value decomposition to the measurement matrix $\mathbf{P} = \mathbf{U}\mathbf{S}\mathbf{V}^\dagger$, Eq. (4.4) takes the diagonal form

$$\mathbf{I}' = \mathbf{S}\mathbf{r}', \tag{4.5}$$

where $\mathbf{r}' = \mathbf{V}^\dagger\mathbf{r}$ and $\mathbf{I}' = \mathbf{U}^\dagger\mathbf{I}$ are the normal modes of the problem and the corresponding transformed data, respectively. The singular values $\mathrm{S_{kk}}$ are the eigenvalues associated with the normal modes, so the relative sensitivity of the tomography to different normal modes is given by the relative sizes of the corresponding singular values. With the help of Eqs. (4.4) and (4.5), the errors are readily propagated form the detection $\mathbf{I}$ to the reconstruction $\mathbf{r}$.

Drawing an analogy between Eq. (4.5) and the filtering by a linear spatially invariant system, the singular spectrum S_{kk} and the sum of the singular values $\sum_k \mathrm{S}_{kk}$ are the discrete analogs of the modulation transfer function and the maximum of the point spread function, respectively. Hence we define the dynamical

range (or field of view) of the SH tomography as the set of normal modes with singular values exceeding a given threshold. The sum of the singular values then describes the overall performance of the SH tomography setup. When some of the singular values are zero, the tomography is not informationally complete and the search space must be readjusted.

For the data in Fig. 4.3, the singular spectrum is shown in Fig. 4.4. Depending on the threshold, around 20 out of the total of 49 modes spanning the space of 7×7 coherence matrices can be discriminated. The modes outside this field of view are mainly those with significant intensity contributions out of the rectangular regions of the CCD sensor. Further improvements can be expected by exploiting the full CCD area and/or using a CCD camera with more resolution, at the expense of more computational resources for data post-processing.

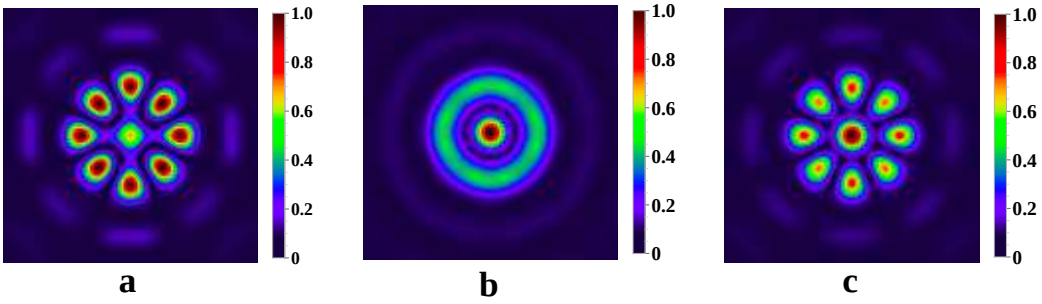

Figure 4.5: **Influence of the spatial coherence on the far-field intensity distribution.** We have considered different mixtures of the modes $|V_4\rangle$, $|V_{-4}\rangle$, and $|V_0\rangle$ and calculated the associated intensity distribution as a Fraunhofer diffraction pattern. (a) fully coherent superposition $|V_4 + V_{-4} + 0.4V_0\rangle\langle V_4 + V_{-4} + 0.4V_0|$; (b) incoherent mixture $|V_4\rangle\langle V_4| + |V_{-4}\rangle\langle V_{-4}| + 0.4|V_0\rangle\langle V_0|$; and (c) partially coherent mixture $|V_4 + V_{-4}\rangle\langle V_4 + V_{-4}| + 0.4|V_0\rangle\langle V_0|$.

4.3 3D Imaging

Once the feasibility of the SH tomography has been proven, we illustrate its utility with an experimental demonstration of 3D imaging (or digital propagation) of partially coherent fields. As it is well known [134], the knowledge of the transverse intensity distribution at an input plane is, in general, not sufficient for calculating the transverse profile at other output plane. Propagation requires the explicit form

of the mutual coherence function G_{in} at the input to determine I_{out}:

$$I_{\text{out}}(\mathbf{x}) = \iint_{-\infty}^{\infty} h(\mathbf{x},\mathbf{x}')h^*(\mathbf{x},\mathbf{x}'')\, G_{\text{in}}(\mathbf{x}',\mathbf{x}'')d\mathbf{x}'d\mathbf{x}''\,. \tag{4.6}$$

Here $\mathbf{x}'$ ($\mathbf{x}''$) and $\mathbf{x}$ are the coordinates parametrizing the input and output planes, respectively, and $h(\mathbf{x},\mathbf{x}')$ the response function accounting for propagation. The dependence of the far-field intensity on the beam coherence properties is evidenced in Fig. 4.5 for coherent, partially coherent and incoherent superpositions of vortex beams.

Once the coherence matrix is reconstructed, the forward/backward spatial propagation can be obtained using tools of diffraction theory and, consequently, the full 3D spatial intensity distribution can be computed. In particular, the intensity profile at the focal plane of an imaging system can be predicted from the SH measurements. This has been experimentally confirmed, as sketched in Fig. 4.6. We prepared the partially coherent vortex beam $|V_4+V_{-4}\rangle\langle V_4+V_{-4}|+k|V_0\rangle\langle V_0|$, where k was a parameter governing the degree of spatial coherence. To this end, a coherent mixture $|V_4+V_{-4}\rangle\langle V_4+V_{-4}|$ was realized by the digital-holography part of the setup, whereas the zero-order vortex beam $|V_0\rangle$ was prepared by removing the spiral phase mask. The output diameter of the beam was set to 4.9 mm. The reconstructed coherence function (upper left) was digitally propagated to the focal plane of a lens and the intensity distribution at this plane was calculated (upper right) and compared with the actual CCD scan in the same plane (lower right). Excellent agreement between the predicted and measured distributions was found.

The measurement was done in three steps. First, the SH sensor (see Fig. 4.1) was replaced by a lens of 500 mm focal length and the far-field intensity was detected at its rear focal plane with a CCD camera (Olympus F-View II, 1376×1032 pixels, 6.45 μm×6.45 μm each). Second, the same vortex superposition was subject to the SH tomography using the SH sensor (Flexible Optical) and the reconstruction of the coherence matrix in the 7-dimensional subspace spaned by the vortices V_ℓ with $\ell \in \{-6,-4,-2,0,+2,+4,+6\}$. Once $\boldsymbol{\rho}$ is reconstructed, the far-field intensity was computed using Eq. (4.6), where the focusing is described by the Fraunhofer diffraction response function. The predicted intensity was found to be in an excellent agreement with the direct sampling by the Olympus CCD camera. Finally, the Flexible Optical SH sensor was replaced by a HASO3 SH detector. The intensity and wavefront of the prepared vortex beam was measured and the far-field intensity was computed by resorting to the transport of intensity equation [135, 136] performed by the HASO software. Resampling was done to match the resolution of the HASO output to the resolution of the Olympus CCD camera.

We emphasize that the standard SH operation fails in this kind of application [137]. To quantify the result, we compute the normalized correlation coef-

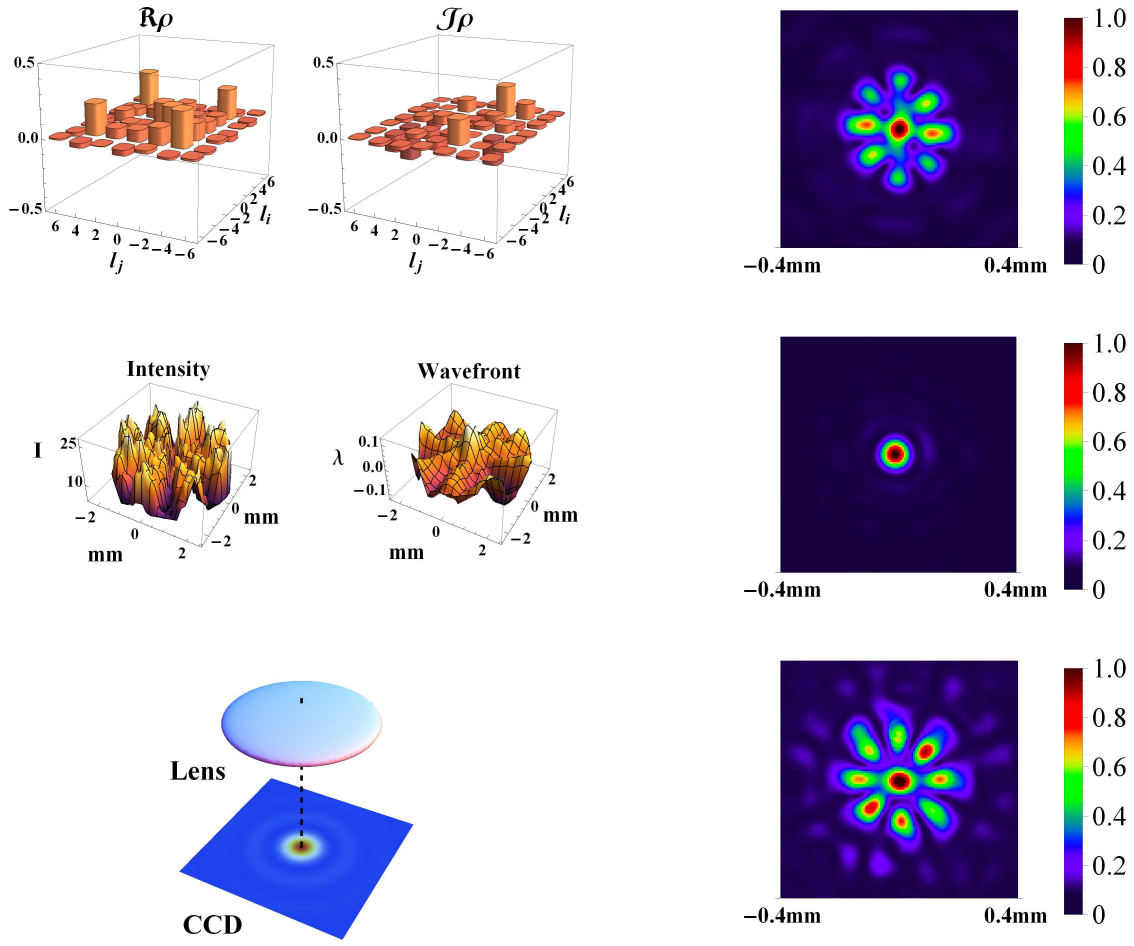

Figure 4.6: **Digital 3D imaging.** The prediction of the far-field intensity distribution is compared with a direct intensity measurement. The partially coherent vortex beam $|V_4+V_{-4}\rangle\langle V_4+V_{-4}|+k|V_0\rangle\langle V_0|$ was generated (with a beam diameter of 4.9 mm) with a fixed parameter k (unknown prior to the reconstruction). . Upper, middle and lower pannels correspond to the SH tomography, standard SH measurement and direct intensity measurement, respectively. Upper left: Real and imaginary parts of the reconstructed ρ in the 7-dimensional space spanned by the vortices V_ℓ with $\ell \in \{-6,-4,-2,0,2,4,6\}$. Upper right: Calculated far-field intensity distribution I_ρ based on the reconstructed ρ propagated to the focal plane of the lens ($f = 500$ mm). Middle left: Intensity distribution (in arbitrary units) and wavefront as measured by the standard SH sensor. Middle right: Calculated far-field intensity distribution I_{std} using the standard SH wavefront reconstruction and the transport of intensity equation included in the sensor (HASO$^{\text{TM}}$). Bottom left: Schematic picture of the direct intensity measurement at the lens focal plane. Bottom right: The result of the direct intensity measurement I_{CCD} at the focal plane with a CCD camera.

ficient $[C(I_a,I_b) = \sum_{i,j} I_a I_b / \sqrt{\sum_{i,j} I_a^2}\sqrt{\sum_{i,j} I_b^2}]$ of the measured intensity with the prediction: the result, $C(I_{\text{std}},I_{\text{CCD}}) = 0.47$, confirms the inability of the standard SH to cope with the coherence properties of the signal. This has to be compared with the result for the SH tomography: $C(I_\rho,I_{\text{CCD}}) = 0.89$, which supports its advantages.

Even in the case of fully coherent signal, complex amplitude of vortex beam is difficult to reconstruct with the standard SH reconstruction. Another experiment with the 3D imaging of vortex beam was carried out to prove the ability of proposed technique to deal with such kind of signals. Consider the one-parameter family of Laguerre-Gaussian (LG) modes with no radial nodes specified by the orbital angular momentum quantum number l, $\langle s,\varphi|\text{LG}_l\rangle \propto s^l \text{e}^{\text{i}l\varphi}\text{e}^{-s^2}$.

The preparation was targeted at creating a superposition of moderately-high-order LG modes: $\rho^{\text{true}} \approx |LG_4 + LG_8\rangle\langle LG_4 + LG_8|$. The proposed reconstruction method was used to reconstruct the coherence matrix in the chosen 11-dimensional space spanned by the 11 lowest-order LG modes. In total there was 121 real parameters to reconstruct.

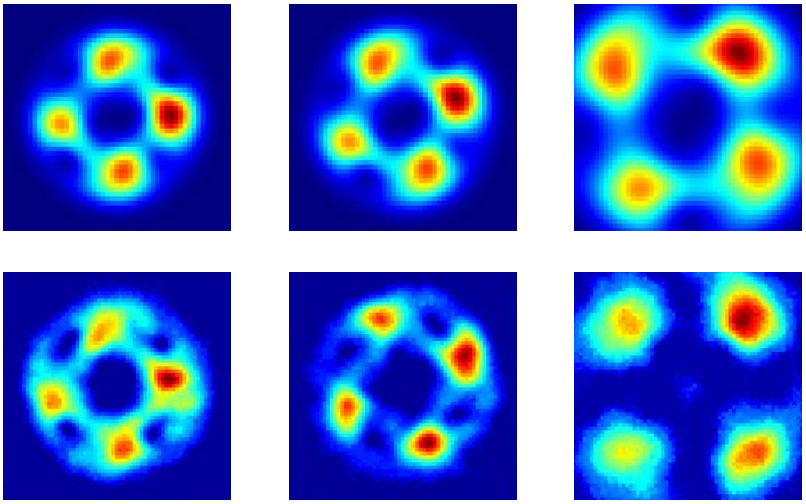

Figure 4.7: 3D imaging of a coherent vortex beam superposition. Predicted (top) and measured (bottom) intensity distributions are shown at the SH sensor (left), and 17cm (middle) and 62cm (right) further down the beam.

The analysis was done in three steps. First, the coherence matrix ρ^{rec} of the measured signal was reconstructed. Second, the intensity distribution was calculated from ρ^{rec} and compared to the CCD scan. Third, ρ^{rec} was numerically propagated 62cm from the SH plane and the corresponding intensity was compared to

the experimentally measured intensity at the same plane. Figure 5.1 shows a very good agreement between the reconstructed and measured images across the 62cm range. Non-symmetric intensity distribution is successfully reconstructed and its rotation during the beam spreading is revealed as well.

4.4 Incomplete SH tomography

Finally, we make use of the MLME algorithm to reconstruct states of classical light beams that are measured using the Shack-Hartmann (SH) wave front sensor. Since coherence operator ρ_{coh} possesses all the properties of a statistical operator, the MLME technique can be used to estimate the true coherence operator $\rho_{\mathrm{coh}}^{\mathrm{true}}$ of a partially coherent beam.

The aforementioned set-up is used for generating and analyzing low-order Laguerre-Gaussian (LG) modes. The LG modes can serve as important resources in quantum information processing [138]. In this experiment, only LG modes with no radial nodes are considered. Such modes form a one-parameter orthonormal basis, where the modes are specified by the orbital angular momentum quantum number l. In polar coordinates, the relevant part of the complex amplitude of a LG mode, for a fixed l, is given by

$$\langle s, \varphi | \mathrm{LG}_l \rangle \propto s^l \mathrm{e}^{\mathrm{i}l\varphi} \mathrm{e}^{-s^2} . \tag{4.7}$$

Nonzero values of l give rise to helical wave fronts, for which each photon carries an orbital angular momentum of $l\hbar$.

For the source of light beams, we would like to prepare the state $\rho_{\mathrm{coh}}^{\mathrm{true}} = \rho_{\mathrm{coh}}^{\mathrm{sup}} = |\psi_{\mathrm{sup}}\rangle\langle\psi_{\mathrm{sup}}|$, where

$$|\psi_{\mathrm{sup}}\rangle = (|\mathrm{LG}_0\rangle - |\mathrm{LG}_1\rangle \mathrm{i} - |\mathrm{LG}_2\rangle) \frac{1}{\sqrt{3}} , \tag{4.8}$$

using the OPTO SLM. In the presence of experimental imperfections, however, the true state $\rho_{\mathrm{coh}}^{\mathrm{true}}$ prepared this way will not be exactly the same as $\rho_{\mathrm{coh}}^{\mathrm{sup}}$. After measuring this beam with the SH sensor, the data are processed using the MLME algorithm in Eq. (3.18) to obtain the estimator $\hat{\rho}_{\mathrm{coh}}^{\mathrm{MLME}}$ for $\rho_{\mathrm{coh}}^{\mathrm{true}}$, since $G < 1$. To quantify the quality of $\hat{\rho}_{\mathrm{coh}}^{\mathrm{MLME}}$, we investigate the *fidelity* between $\hat{\rho}_{\mathrm{coh}}^{\mathrm{MLME}}$ and $\rho_{\mathrm{coh}}^{\mathrm{sup}}$. Figure 4.8 shows the CCD image for the state $\rho_{\mathrm{coh}}^{\mathrm{true}}$. Each aperture gives rise to a bright spot in the CCD image. To maximize the signal-to-noise ratio, only the pixel with the highest intensity within each spot is selected as a measurement datum. The set of intensities, corresponding to maximum-intensity pixels, constitute the measurement data to be used for state reconstruction. In our case, the corresponding POM consists of 35 linearly independent outcomes described by

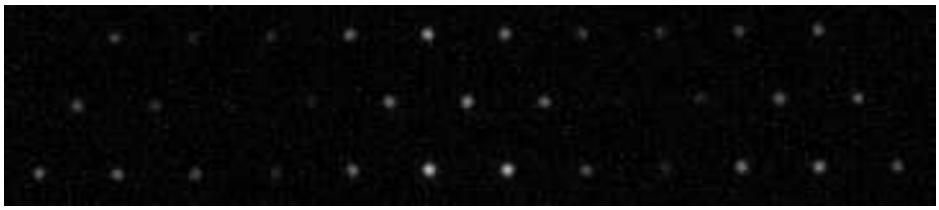

Figure 4.8: CCD image for the state $\rho_{\mathrm{coh}}^{\mathrm{true}}$. The relevant part of the SH readout used for the beam reconstruction is shown. Contributions from the individual SH apertures are indicated by bright spots, with each spot made up of multiple pixels. Note that the two void regions correspond to the phase singularities of the state $\rho_{\mathrm{coh}}^{\mathrm{sup}}$. This hints that $\rho_{\mathrm{coh}}^{\mathrm{true}} \approx \rho_{\mathrm{coh}}^{\mathrm{sup}}$.

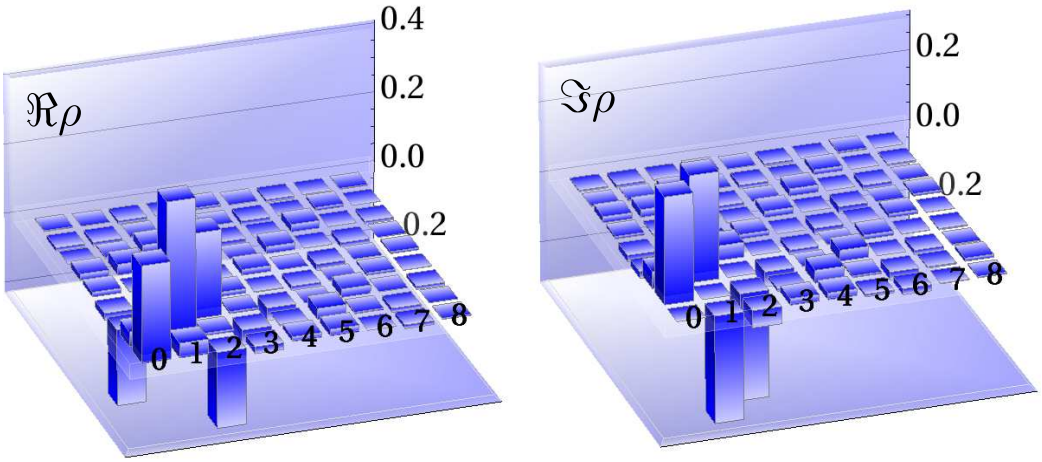

Figure 4.9: MLME state estimation from informationally incomplete data for $D_{\mathrm{sub}} = 9$. The real (left) and imaginary (right) parts of the reconstructed coherence operator $\hat{\rho}_{\mathrm{coh}}^{\mathrm{MLME}}$ are shown. The reconstruction subspace is spanned by the modes LG_l, with $l = 0, 1, \ldots, 8$. In this case, 56 out of 91 independent outcomes, required for complete characterization of $\rho_{\mathrm{coh}}^{\mathrm{true}}$, are not accessible, yet the MLME estimator $\hat{\rho}_{\mathrm{coh}}^{\mathrm{MLME}}$ is close to $\rho_{\mathrm{coh}}^{\mathrm{sup}}$, with a fidelity of 92%.

Eq. (3.25). This measurement is, therefore, informationally complete for $D_{\mathrm{sub}} \leq 5$. In cases where state reconstruction on informationally complete subspaces gives unsatisfactory results, the MLME approach can be used on the informationally incomplete data to give reasonable estimators on a larger subspace, as illustrated in Fig. 4.9.

So far, the procedure of state-space truncation is performed in the basis of the

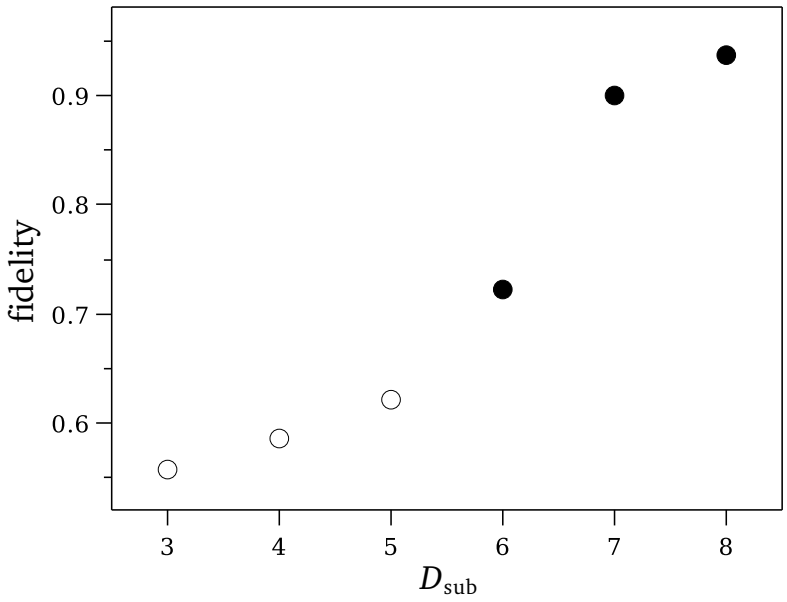

Figure 4.10: Average fidelities, computed over 50 random choices of computational bases, of the estimators for different dimensions D_{sub} of the reconstruction subspace. The unfilled (filled) circular plot markers correspond to informationally complete (incomplete) tomography, respectively.

LG_l modes. In this basis, when $\rho_{\mathrm{coh}}^{\mathrm{true}}$ is known to be quite close to $\rho_{\mathrm{coh}}^{\mathrm{sup}}$, the truncation of modes of higher orders will not result in a great loss of reconstruction information, as implied by the structure of $\rho_{\mathrm{coh}}^{\mathrm{sup}}$ in Eq. (4.8). The situation will be very different when there is no such prior knowledge about $\rho_{\mathrm{coh}}^{\mathrm{true}}$, except for the fact that the possible values of l lie in a certain range. In this situation, there is no appropriate strategy to choose a computational basis in which the state-space truncation can be done effectively and justifiably. More generally, estimating the unknown state $\rho_{\mathrm{coh}}^{\mathrm{true}}$ on a truncated subspace will, as a rule, result in missing important reconstruction information and this will lead to strongly biased estimators. A remedy for this problem is to perform state reconstruction on a sufficiently large subspace that is compatible with the knowledge about the range of values of l.

To emphasize this point, we simulate the following scenario:

- The set of measurement data, obtained from the CCD image shown in Fig. 4.8, is distributed to 50 parties. The possible values of l for the true state $\rho_{\mathrm{coh}}^{\mathrm{true}}$ are known to lie in the range $l \in [0,7]$.
- Each party selects a computational basis and estimates the state of the beam for $D_{\mathrm{sub}} = 3,4,\ldots,8$ using either the ML (for $D_{\mathrm{sub}} \leq 5$) or the MLME algorithm (for $D_{\mathrm{sub}} > 5$).

- The reconstructed estimators for the six values of D_{sub} are reported by each party and the average fidelity of the estimators for every value of D_{sub} are calculated.

A typical outcome of this scenario is shown in Fig. 4.10. As can be seen, performing state-space truncations in order to reconstruct $\rho_{\text{coh}}^{\text{true}}$ with an informationally complete set of data generally leads to low fidelities in the estimators. Increasing the number of degrees of freedom and using the MLME algorithm to cope with the completeness issue seems to be a much better strategy.

4.5 Discussion

We have demonstrated a nontrivial coherence measurement with a SH sensor. This goes further the standard analysis and constitutes a substantial leap ahead that might trigger potential applications in many areas. Such a breakthrough would not have been possible without reinterpreting the SH operation as a simultaneous unsharp measurement of position and momentum. This immediately allows one to set a fundamental limit in the experimental accuracy [139].

Moreover, although the SH has been the thread for our discussion, it is not difficult to extend the treatment to other wavefront sensors. For example, let us consider the recent results for temperature deviations of the cosmic microwave background [140]. The anisotropy is mapped as spots on the sphere, representing the distribution of directions of the incoming radiation. To get access to the position distribution, the detector has to be moved and, in principle, such a scanning brings information about the position and direction simultaneously: the position of the measured signal prior to detection is delimited by the scanning aperture, whereas the direction the signal comes from is revealed by the detector placed at the focal plane. When the aperture moves, it scans the field repeatedly at different positions. This could be an excellent chance to investigate the coherence properties of the relict radiation. To our best knowledge, this question has not been posed yet. Quantum tomography is especially germane for this task.

Let us stress that classical estimation theory has been already applied to the raw SH image data, offering an improved accuracy, but at greater computational cost [141, 142]. However, the protocol used here can be implemented in a very easy, compact way, without any numerical burden.

Finally, the iterative algorithms for informationally incomplete estimation respectively for perfect and imperfect measurements was applied to wavefront tomography of Laguerre-Gaussian beams. We learned that one should better not restrict the state reconstruction to a subspace in which the relevant measurements are informationally complete. Doing so can result in reconstruction artifacts that

originate in the state-space truncation and may result in inaccurate estimators for the unknown true state. Instead, one should perform the reconstruction on a larger subspace, with additional unsampled degrees of freedom, that is compatible with any prior information about a given unknown state. Such a more objective way of state estimation results in a much better tomographic quality of the reconstructed estimator.

Chapter 5

Data pattern tomography: Reconstruction with unknown apparatus

This chapter is motivated by a simple question: Is it really necessary to know *all* the measurement device before the reconstruction starts? Intuitively, it is clear that since the supposedly signal state is localized in some region of the search subspace, one can be satisfied with device features associated with probing only this region. Then it is sufficient calibrating the device only in this region. The question is how to distinguish these features having no *a-priori* information about the signal state and relying only on results of measurements performed on the signal state.

Surprisingly, there is a simple way how to do this. It will be shown that the calibration can be incorporated in the reconstruction process. Information about the device can be updated on the basis of the reconstruction results obtained in each step of the estimation procedure. In this sense this proposal reminds adaptive algorithms known as "neural networks," when self-learning is an important part of the reconstruction protocol. Here we will discuss such an adaptive reconstruction scheme based on the recently formulated pattern tomography [79]. This scheme makes use of fitting measurement data obtained for an unknown signal state on the set of data obtained for known probe states. It does require neither calibration of the measurement nor any assumptions about the search subspace, which is naturally defined by the choice of probe states. Such a reconstruction procedure was shown to be analogous to the classical image processing [143]. Here we elaborate further this idea into a versatile and economical tool that provides means to make quantum state estimation tomography without knowledge about the measurement apparatus using limited quasi-classical resources.

First we demonstrate how a general quantum state can be represented as a

mixture of quasi-classical coherent and thermal states with positive and negative weights. We describe the procedure of constructing such a representation with a minimal number of appropriately chosen known quasi-classical states. Particularly, it will be shown that the single-photon state can be represented with arbitrary accuracy with just two thermal states.

Then, we develop an estimation procedure implementing adaptive choice of probe states for improved fit and more precise estimation. New probe states are selected using available data patterns in adaptive fashion. We also demonstrate that the proposed data pattern reconstruction is experimentally feasible and particularly well suited for inference of photon-number distributions.

5.1 Representation by mixtures of classical states

The key point in our discussion is a possibility to represent an arbitrary quantum state as a mixture of appropriately chosen states with positive and negative weights. The density matrix, ρ, of the signal state is supposed to be represented as a mixture

$$\rho = \sum_{j=1}^{N} x_j \sigma_j, \tag{5.1}$$

where the coefficients x_j are real scalars (not necessarily positive) and σ_j are density matrices describing a set of linearly independent (generally, nonorthogonal) probe states. For the concreteness, let us assume Gaussian probe states, namely, coherent or thermal states.

Discrete representation (5.1) represents a generalization of the concept of P-representation [144] and can be sufficiently accurate depending on the number of terms in the sum. Notice that for calculating averages with arbitrary precision, one can approximate even highly singular P-function by an infinitely differentiable function [146]. Then, the sufficiently dense discretization can be adopted for required approximation of the state analogously to Refs. [147]. Coherent state projectors used for P-representation can be replaced by continuous representation of arbitrary Gaussian operators [148].

Here we suggest to use appropriately chosen non-orthogonal basis unconnected with the quasi-probability discretization. Moreover, that basis of Gaussian density matrices might be very different from the set obtained as the result of the discretization (here it is useful to mention a curious example of representing a thermal squeezed state with few coherent projectors localized in two circles on the phase plane [149]).

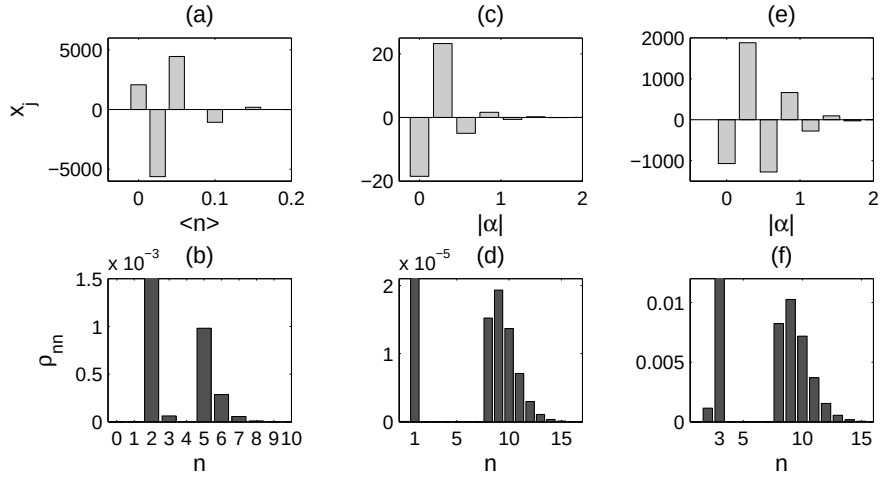

Figure 5.1: Examples of representing quantum states by thermal and phase-averaged coherent basis states (5.3). Panels (a,b) represent coefficients x_j and matrix elements of the two-photon Fock state approximated by $N = 5$ thermal states (distance (5.2) is about 0.0015); panels (c,d) represent the single-photon state with $N = 8$ phase-averaged coherent states, $d = 2.96 * 10^{-5}$. Panels (e,f) represent coefficients x_j and matrix elements of the approximated three-photon Fock state for $N = 8$ phase-averaged coherent basis states, $d = 0.0157$. Note that the panels (b),(d), and (f) are zoomed in on the very small deviations from the state being represented.

5.1.1 Representing phase-averaged states

Let us start with a simple case of states, which are diagonal in the Fock-state representation. Despite its simplicity, this case is highly relevant for the quantum state diagnostics with conventional single-photon detectors. In particular, such representation can be applied for inferring photon-number distributions of a signal state using on/off TMD detection schemes [150–152]. This will be considered in the next section.

First of all, we notice that weak phase-averaged quantum states can be efficiently represented as a mixture of just a few thermal states. Indeed, a single-photon Fock state can be represented as a difference of two weak thermal states. For example, subtracting a vacuum state from a thermal state with $\langle n \rangle << 1$, up to the normalization factor one gets

$$\rho \approx \sum_{n=0} \langle n \rangle^n |n+1\rangle\langle n+1|,$$

where the vector $|n\rangle$ denotes the Fock state with n photons. Similarly, one can

represent Fock states with larger number of photons. In Figs. (5.1)(a,b) an illustration is shown of the two-photon Fock state representation with just five weak thermal states. Here we use the distance

$$d = \sqrt{\sum_{k,l=0} |\rho_{kl}^{est} - \rho_{kl}^{true}|^2} \tag{5.2}$$

for characterizing the quality of the representation, where ρ^{est} is the approximated density matrix and ρ^{true} is the true one; elements ρ_{kl} are taken in the Fock-state basis.

Thermal states are not the only choice for experimentally feasible representation of diagonal states. Phase-averaged coherent states

$$\sigma_j = \sum_{k=0} \frac{|\alpha_j|^{2k}}{k!} e^{-|\alpha_j|^2} |k\rangle\langle k|. \tag{5.3}$$

can be used as well, as has been already demonstrated with Fig. (5.1). Again, a small number of phase-averaged coherent states is sufficient for obtaining a reasonably accurate representation of weak diagonal states. In difference with the thermal-state representation, state with larger average numbers of photons can be used.

Simulation in this subsection were made using the standard procedures of least square fitting. Notice that even for a comparatively small number of terms in the representation ($\simeq 10$) problems of bad conditioning might arise making the straightforward least square procedure problematic (the same kind of problems are plaguing attempts to implement a direct matrix inversion for the reconstruction, see, for example, [150]). However, imposing linear constraints, such as requirement of positivity of the diagonal elements of the density matrix in the Fock state basis and unit trace of them stabilizes the least square fit.

5.1.2 Designing an iterative approximation

For representations discussed in the previous subsection, a predefined small set of phase-averaged or thermal states was used. However, choice of this set is not a trivial task. For the given number of probe states, the quality of representation depends rather strongly on the choice of amplitudes or temperatures (see Fig.5.2). For choosing them we have developed a simple and rather general iterative approach. First of all, we specify a set of available probe states. For phase-averaged signal states considered in this section this set is represented by sequence of coherent state amplitudes or average numbers of thermal photons. For example, it can be an equidistant grid with the distance between neighboring points corresponding to the average photon number difference difference between the corresponding

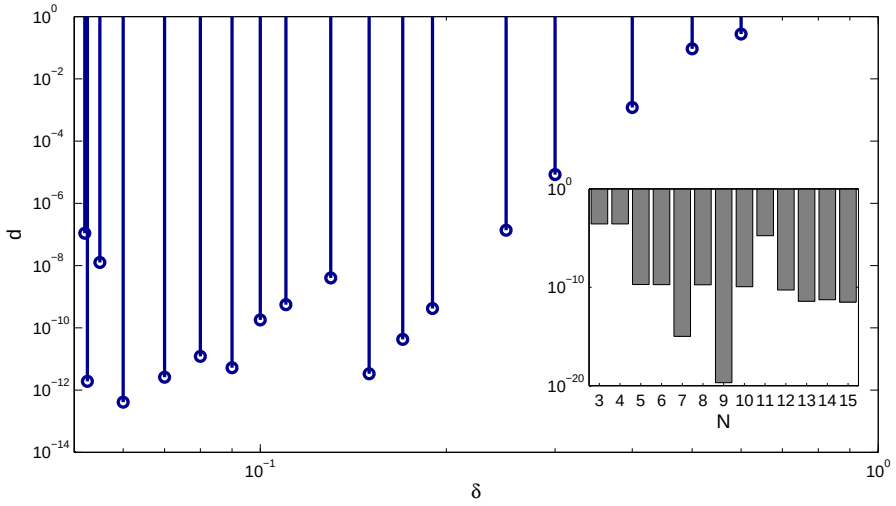

Figure 5.2: Illustration of dependence of the two-photon Fock state representation quality (i.e. parameter d of Eq.(5.2) on the distance between neighbor phase-averaged coherent probe states on the grid, δ. Total 8 probe states were used. Inset demonstrates the performance of the simple iterative fit procedure. There it is shown the dependence of d for the two-photon signal state on the total number of phase-averaged coherent probe states, N. The distance $\delta = 0.1$.)

states much less than the unity (since we are interested here in the reconstruction of signal states with few photons on average). In Fig.5.2 one can see an example of how the quality of the two-photon Fock signal state representation with phase-averaged coherent states depends on the choice of the grid, described by the distance between neighboring points, δ. As it should be expected, when δ remains much less than unity, the representation is good (however, the quality can be changed by orders of magnitude by adding just one state). When the step approaches unity, the representation deteriorates.

Then, we specify the starting point (for example, the vacuum). We have considered two possible ways to develop a fit. The first one is the simplest: we add consecutive points on the grid and see how the fit improves checking residuals. The result of this procedure is shown in the inset of Fig.5.2, where the quality of representation is depicted as a function of the number of probes It it can be seen that just a few of them are sufficient to represent accurately a probe state with no more than a few photons on average. However, one should also notice that the quality of the representation changes in a rather non-monotonous way with adding more probe states (actually, by orders of magnitude). This points to the conclusion that it might be better to modify the iterative procedure as to look for better choice

of probe states rather than increase their number. The procedure can be imagined as follows: firstly, one specifies the number of states on a grid to be used for representation and chooses them within some interval of amplitudes/temperatures (generally, corresponding to probe states with no more than few photons), then tries to replace one of the state with the another state on the grid to achieve better fit.

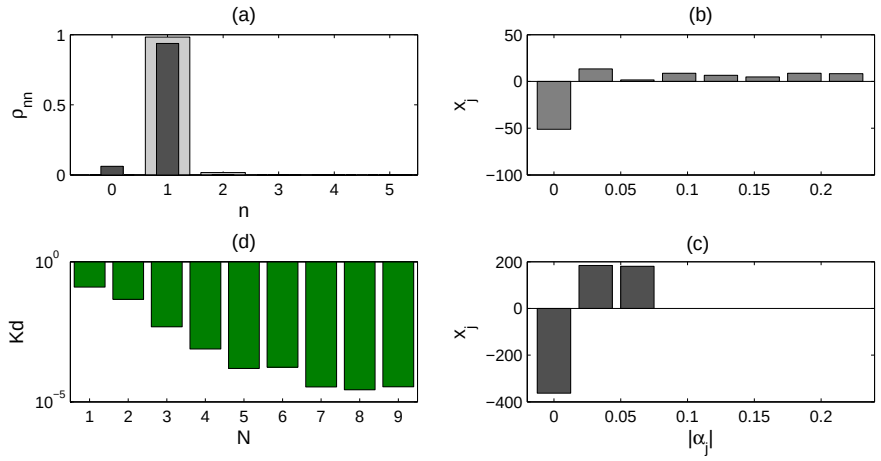

Figure 5.3: Reconstruction of the single-photon Fock state by an iterative procedure described in the text. Phase-averaged coherent probe states are used. (a) Reconstructed photon-number distributions for $N = 8$ probe states (grey bars) and $N = 3$ probe states (black bars). Panels (b,c) show coefficients x_j and amplitudes of the probe states for $N = 8$ (b) and $N = 3$ (c). Panel (d) shows Kullback-Leibler divergence Eq. (5.5) for different number of probe states N. In total, 30 detector efficiencies were used for the reconstruction equidistantly distributed in the interval $[0.1, 0.9]$ and 10^5 copies were measured for each of those settings. The estimation was performed using standard OCTAVE and Mathematica packages for the linearly constrained least squares estimation.

5.2 Reconstruction of a photon-number distribution

Consider now the reconstruction of a photon-number distribution using the data-pattern scheme. As will be shown in sec.3.1.3, the proposed scheme is feasible, efficient, fast, and allows to avoid a meticulous and difficult procedure of calibrating the detection device at the single-photon level. The photon-number inference is performed using a measurement sensitive to the diagonal elements of the den-

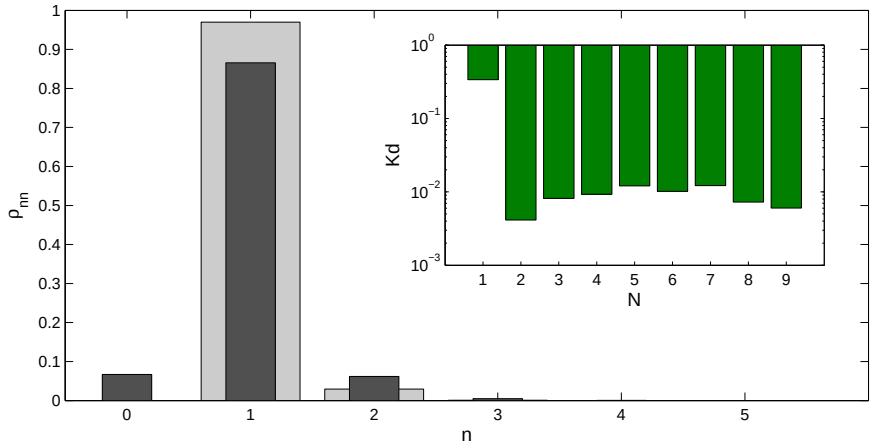

Figure 5.4: Reconstruction of the single-photon Fock state by an iterative procedure using thermal probe states and using POVM elements for the loop TMD detector scheme. Light grey bars correspond to $N = 9$, dark-grey bars correspond to $N = 5$ thermal probe states. The loop on/off detector scheme with 16 POVM elements is considered [153]; 10^5 measurements were taken for each POVM element; for the reconstruction an equidistant set of $\langle n \rangle$ was taken, difference between the neighboring points is $\delta = 0.03$. The inset shows the behavior of the Kullback-Leibler divergence (5.5) in dependence of N.

sity matrix expressed in the Fock-state basis:

$$p_j = \sum_n \Pi_{jn} \rho_{nn}. \tag{5.4}$$

A well-known example of such a measurements (5.4) is the already well-established on/off detection and its modifications [150–152]. Simulated data pattern reconstructions with the simplest version of the on/off detection device are presented in Fig. 5.3. Absorbers are placed before the single-photon detector to change the quantum efficiency of the detection. The data is comprised by the number of clicks detected for each efficiency setting for a sequence of identical copies of the signal state.

An example of the data pattern reconstruction from simulated data using the iterative procedure from the subsection 5.1.2 is shown in Fig. 5.3. The suggested operational procedure is the following: At first the responses to the signal state are recorded. Then patterns generated by a set of probe states are recorded and the reconstruction of the signal is done. The quality of the fit is characterized by introducing a cost function characterizing a difference between measurement outcomes and probabilities predicted by the estimation. In the next iteration, more

probe states are used and new fit is analyzed. The choice of new probe states goes as it was described in the previous section: one is either adds more states from a pre-defined set found sufficient for representation of a wide range of signal states (for example, a new row or column from the set defined on a square lattice), or uses results of the previous step to find the best probe states to be added (somewhat similarly to as was done in the adaptive procedure described in the previous section; the important difference that we want incorporating all the previously measured probe states into the fit). The procedure stops when the fit does not change significantly upon adding more probe states.

Phase-averaged coherent states were considered as probes. The values of the probe-state amplitudes are taken from the predefined equidistant lattice with a period much smaller than unity (which can be considered rather general rule for the case, since we are interested in the reconstruction of few-photon signals); $\delta = 0.02$ for the example. The vacuum state was chosen as a starting points, on each subsequent step of the procedure the next probe state on the grid was added. The Kullback-Leibler divergence

$$Kd = \sum_j f_j \log\left\{\frac{f_j}{p_j}\right\} \tag{5.5}$$

is used as a cost function quantifying the quality of the fitting procedure. Here f_j are the measured frequencies for the signal state, and p_j are the probabilities predicted from the reconstructed state. Notice that the photon-number distribution of a single photon state can be reconstructed with just a few semi-classical probe states. Also notice that the information about the actual detector efficiencies was not used in the estimation process. It can be seen that adding more responses from additional probe states would typically improve the fit (Fig.5.3(d)), although some oscillations of the quality with adding new terms might also occur.

Possible non-monotonous character of the quality of the fit can be well illustrated with reconstruction based on thermal probe states. Results for the single-photon state estimation with thermal probe states and a realistic fiber-loop TMD detector (see sec.3.4) are shown in Fig. 5.4 [153, 154]. In the loop detector, the signal travels several times round the fiber loop. Each time a portion of the signal is split off at a fiber beam splitter and gets detected at the single-photon detector with on/off result. For M passes, 2^M different outcomes are thus registered. One can see in Fig.5.4 that for a single-photon state, quite a precise fit is achieved with just two thermal probe states. With adding more probe states the quality first drops down and improves gradually with adding more probe states. Still, the procedure is efficient in comparison with the full calibration of the measurement set-up, since just a few probe states are needed here.

5.3 Discussion

We have presented the data pattern approach to quantum tomography. It appears that this technique may become an efficient and feasible tool in experimental quantum-state reconstruction, the most prominent feature being the ability to perform reconstruction without ever knowing the exact properties of the measurement apparatus. The knowledge required for the precise estimation of a particular signal state can be obtained *a-posteriori*, after the measurement on the signal state is done. Characterizing the quality of the estimation by means of the Kullback-Leibler divergence, one can decide, which additional probe states might be helpful for further improvement of the reconstruction. This strategy was demonstrated with simulated estimations of the diagonal elements of the density matrix in Fock basis for light pulses using TMD detection . We have explicitly demonstrated that coherent and thermal probe states provide adequate quantum resources even for the reconstruction of highly non-classical signal states with few photons. This is a considerable advantage for the experimenters, since calibrating measurement set-ups for such weak signals can be rather a challenging task.

Chapter 6

Quantum polarization tomography of bright squeezed light

In this chapter, we perform a full tomography reconstruction of the polarization sector of bright polarization squeezed beam starting from a complete set of Stokes measurements, based on theoretical foundations from the section 3.3. The reconstruction is accomplished in three different ways: by the direct inversion of the Radon transform, by a novel maximum-likelihood estimation and, finally, by a Gaussian approximation. We find that the maximum likelihood reconstruction provides significantly higher statistical inversion stability, which allows to get reconstruction of the same quality but from far smaller data set.

6.1 Experimental setup

To validate our approach, we perform the tomography of a polarization squeezed state, generated in a polarization-maintaining optical fibre through the nonlinear Kerr effect [99]. The setup is shown in figure 1. The light source is a shot-noise limited ORIGAMI laser from Onefive GmbH emitting 220 fs pulses at a repetition rate of 80 MHz and centered at 1560 nm. The light is fed into a 13 m-long polarization-maintaining birefringent fibre (3M FS-PM-7811, 5.6 μm mode-field diameter) so that quadrature squeezed states are simultaneously and independently generated in both polarization modes. The strong birefringence of the fibre (beat length 1.67 mm) causes a delay between the emerging quadrature-squeezed pulses. We precompensate for this delay in an unbalanced Michelson-like interferometer placed before the fibre. A small part (0.1 %) of the fibre output serves as the input to a control loop to maintain the relative phase between the exiting pulses locked to $\pi/2$, so the light is circularly polarized.

The quantum state is detected with a Stokes measurement, as sketched in the

previous section. The two detectors (InGaAS PIN photodiodes, custom-made by Laser Components GmbH with 98 % quantum efficiency at DC) are balanced and have a sub-shot noise resolution at a frequency range between 5 MHz and 30 MHz. Each detector has two separate outputs: DC, providing the average values of the photocurrents, and AC, providing the photocurrents amplified in radio-frequency (RF) spectral range. The RF currents of the photodetectors are mixed with an electronic local oscillator at 12 MHz, amplified (FEMTO DHPVA-100), and digitized by an analog/digital exit converter (Gage CompuScope 1610) at 10 Megasamples per second with a 16-bit resolution and 10 times oversampling.

The measurements are performed at a pulse energy of 93 pJ. In the dark plane a total squeezing of about 3.8 dB is observed. In the orthogonal quadrature, the noise was enhanced by several tens of dB due to Guided Acoustic Wave Brillouin Scattering (GAWBS) [155–157]. In the direction of the classical excitation, the state is expected to be shot-noise limited, since the Kerr effect only influences the phase and does not contribute to the photon number.

To perform the reconstruction, histograms of the Stokes variables are recorded for different angles (θ, ϕ). This is done by rotating the wave plates with motorized stages (OWIS DMT 40-D20-HSM) and scanning one eighth of the Poincaré sphere in 8100 steps, a measurement that took over eight hours. The unmeasured octants were deduced from symmetry. For each setting of the wave plates, the photocurrent noise of both detectors was simultaneously sampled 0.5×10^6 times. Noise statistics of the detectors difference current were acquired in histograms with 751 bins. Additionally, the optical intensity was recorded.

In figure 2 we show typical histograms at different angles on the Poincaré sphere. As the widths largely vary from squeezing to antisqueezing ranges, there are two plots in which the amplitude scale differs in more than one order of magnitude. The histograms labeled 1, 2 and 3 are measured in the dark plane. To-

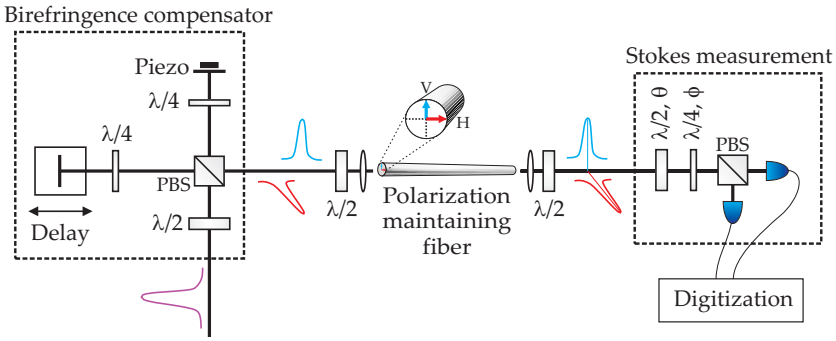

Figure 6.1: Setup for efficient polarization squeezing generation and the corresponding Stokes measurement apparatus.

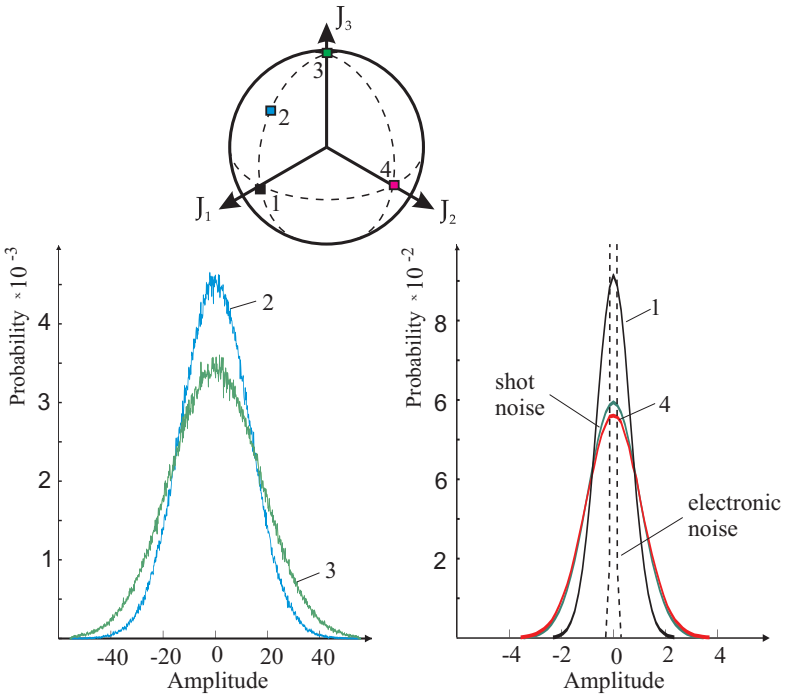

Figure 6.2: Measured histograms of the difference current of the two detectors for various measurement directions on the Poincaré sphere.. Note the different scales on both plots. Histograms 1, 2, and 3 are in the dark plane, while histogram 4 is at the classical mean value. The histograms corresponding to electronic and shot noise are also shown.

mogram 1 denotes the angle of maximum squeezing, while 3 corresponds to the antisqueezing. Tomogram 4 is at the classical mean value, where the measured noise is almost shot-noise limited. Due to the high number of samples, the measured histograms are smooth and, at the same time, the number of bins makes it possible to resolve the large dynamical range of amplitudes, so no data interpolation was needed. We also plot histograms showing the electronic noise and the shot noise.

For all these histograms we have performed a Gaussianity check, using the Kolmogorov-Smirnov and the χ^2 tests, as well as the Kullback-Leibler divergence [158]. We can conclude that all the histogramas are Gaussian within confidence levels ranging from 95 % to 98 %.

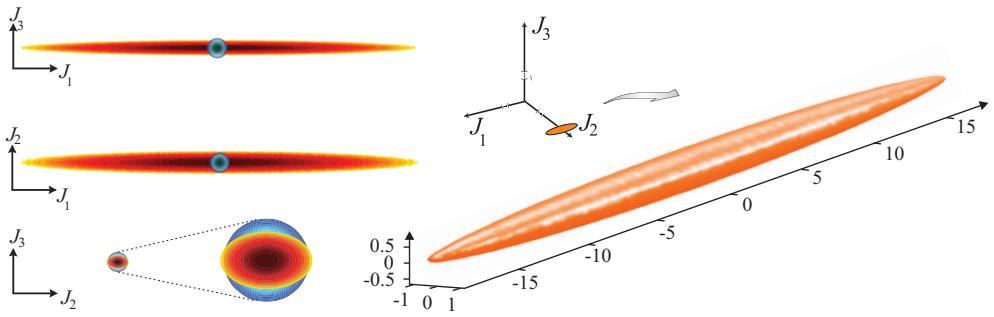

Figure 6.3: (Right) Isocontour surface of the level $1/e$ (from the maximum) of the Wigner function $W(J,\theta,\phi)$ for the polarization squeezed state generated in the setup of figure 1. (Left) Sections of the Wigner function through the three coordinate planes. In blue we show the isotropic section for a coherent state, which we use as unit for all the plots.

6.2 Experimental reconstruction

6.2.1 Inverse Radon reconstruction

As clearly expressed in (3.67), for high photon numbers the tomography turns out to be equivalent to an inverse Radon transform of the measured histograms. In practice, this one-step 3D reconstruction is very demanding in computational resources. Therefore, we divide the process into two steps: first, a set of 2D projections is reconstructed from the recorded histograms; subsequently, the Wigner function is slice-wise generated from those projections (to which we apply a Hamming filter to smooth the noise). The symmetry of the state is used as a prior information to reduce the range of measured angles to an octant. This minimizes the systematic errors stemming from imperfections of the polarization optics.

In figure 3 (right panel) we show the final result of the inverse Radon transform for our polarization squeezed state. More concretely, we plot an isocontour surface of $W(J,\theta,\phi) =$ constant (with the constant being $1/e$ from the maximum) in the Poincaré space having J_1, J_2, and J_3 as orthogonal axes. As coordinate units we use the shot noise set by a coherent state. The ellipsoidal shape of the state is clearly visible. The center of the ellipsoid is far away from the origin, since we have 10×10^{11} photons per measurement time (using 1.9 MHz resolution bandwidth). The antisqueezed direction of the ellipsoid is dominated by excess noise stemming largely from GAWBS, as we have already mentioned.

In the left panel of figure 3 we sketch density plots of the projections on the coordinate planes of the previous Wigner function (including the particular case of a coherent state). The contours agree with the 3.8 ± 0.3 dB squeezing that was directly measured from the variances. The projections on the planes J_1-J_2 and

J_2-J_3 show an additional spreading of the state in the J_2 direction caused by the imperfect polarization contrast in the measurement setup that mixes some of the antisqueezing on the J_2 direction.

This Radon reconstruction requires a large set of measured data to get a reasonably accurate representation of the state. There are two main reasons for this: integrals are approximated by finite sums (in our case, we used 751 bins in 91 steps) and the kernel (3.64) is singular, so some *ad hoc* filtering of the raw data is needed. Acquiring such large data sets may be unwise, for it demands long measurement times. Ensuring the proper stability of the setup is thus essential and might be difficult depending on the quantum state measured.

6.2.2 Maximum-Likelihood reconstruction

This limitation may be circumvented by adopting a statistically-motivated method, such as the maximum likelihood (ML) [159]. In our case, the relation between the Wigner function W and the tomograms w can be written as a system of linear equations

$$w_j = \sum_j c_{jk} W_k, \tag{6.1}$$

where the subscripts in W_k and w_j is a shorthand notation for the respectives coordinates. The coefficients c_{jk} can be interpreted as the overlap of the jth projector with the kth volume element of the Wigner function and can be readily determined from equations (3.53) and (3.60). The most likely Wigner function is then found by minimizing the Kullback-Leibler divergence between the normalized vectors of the computed tomograms w_j and recorded ones $\bar{w}_j$. Technically, this can be achieved by the iterative expectation-maximization algorithm [160–162]

$$W_k^{(n+1)} = W_k^{(n)} \frac{\sum_j w_j}{(\sum_j \bar{w}_j)(\sum_j c_{jk})} \sum_j \frac{\bar{w}_j}{w_j} c_{jk}\,, \tag{6.2}$$

which converges monotonously to the ML estimate from any strictly positive initial vector $W_k^{(0)}$.

The significantly greater stability of the statistical inversion allows us to get reconstructions of the same quality but from far smaller data sets. This is illustrated in figure 4, where we draw a comparison between Radon and ML methods, although in the latter case using only nine different settings of the angles (θ, ϕ), which amounts to reducing the measurements by two orders of magnitude. In other words, the measuring time is shortened from eight hours to less than five minutes! This result indicates that the experimental characterization of considerably more complicated quantum states with less symmetries should still be within the reach of the present measurement setup.

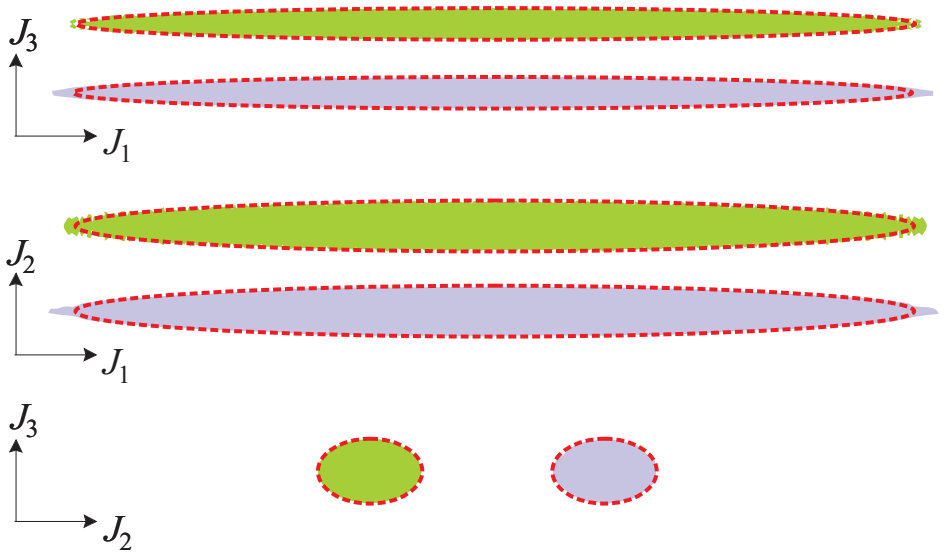

Figure 6.4: Sections of the isocontour of the Wigner function in figure 3 through the coordinate axes, for the three different reconstruction techniques used. In grey, direct Radon transform, in green ML method with nine settings for the angles of the wave plates and in dotted lines the results of a Gaussian ML approximation.

6.2.3 Dark plane reconstruction

As we have discussed in section 3.3.2, the dark plane is of special interest. The theory shows that the reconstruction therein can be obtained in two different ways: either by reconstructing the dark mode directly from the histograms or by calculating projection of the 3D Wigner function along the J_2 direction. The two results are compared in figure 6.5 and good agreement within the experimental uncertainties is found. Since the Radon transform should provide a plausible explanation for all the measured histograms, such a comparison may serve as an independent test of the quality of the 3D tomography.

Finally, the high confidence levels of the Gaussianity tests seems to call for a Gaussian ML reconstruction. The Gaussianity is used as a prior information about the signal, which helps to reduce drastically the number of free parameters. In this case, the Wigner function is represented by the 3×3 covariance matrix G:

$$W(\mathbf{n}) \propto \exp\left(-\frac{1}{2}\mathbf{n}G^{-1}\mathbf{n}\right), \tag{6.3}$$

and the calculated variances $\sigma_j = \mathbf{n}_j G \mathbf{n}_j$ are matched (in the ML sense) to the actually measured variances [163]. Since G must be positive semidefinite, only six real parameters describe the measured system and the problem is highly overdetermined, in consequence, the Gaussian state can be obtained from a few histograms.

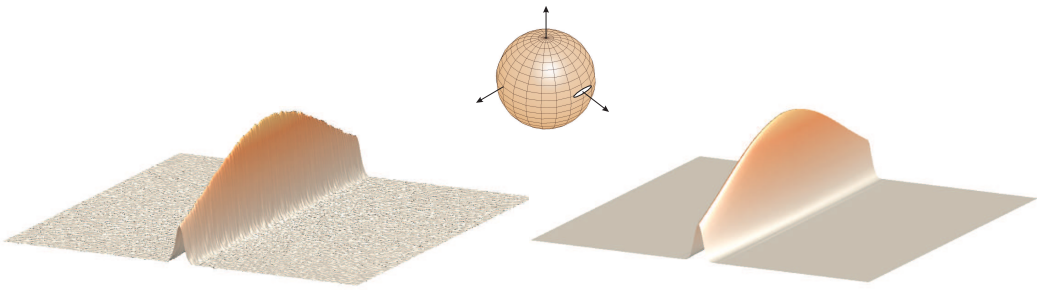

Figure 6.5: Dark plane reconstructions. Left panel: Reconstruction obtained by integrating the Wigner function shown in figure. 3 in the J_2 direction. Right panel: ML reconstruction from dark-plane histograms. Only nine settings of angles θ and ϕ were used for the ML tomography.

In principle, by comparing Gaussian reconstructions based on different subsets of measured data, various imperfections of the setup, such as instabilities and biases, can be detected.

The matrix G turns out to be

$$G = \begin{pmatrix} 3.0920 \times 10^2 & -1.1931 & -2.0160 \\ -1.1931 & 4.4485 \times 10^{-1} & -1.2926 \times 10^{-2} \\ -2.0160 & -1.2926 \times 10^{-2} & 1.1511 \end{pmatrix}, \qquad (6.4)$$

which once diagonalized gives the principal variances 0.43962, 1.13853, and 309.22177 (in shot-noise units). This agrees well with the standard and ML reconstructions, as can be also appreciated in figure 4. The Gaussian reconstruction was done without assuming a particular orientation or symmetry of the state with respect to the Stokes coordinates. The covariance matrix suggests that the misalignment of the principal axis is less than 0.5 degrees within the measurement errors, in accordance with the definition of angles adopted in the experiment.

This Gaussian approach allows for a simple estimate of the errors: just take the pseudoinversion of the measurement matrix as a linear model and use the standard theory of error propagation. The errors to be propagated are actually the errors in the estimated variances for each tomogram, which are found from the χ^2 distribution. In addition, we can assume that the variances of different tomograms are uncorrelated.

Taking a 97.5 % confidence interval (which corresponds to three standard deviations), the principal variances can be written as

$$0.440 \pm 0.002, \quad 1.139 \pm 0.001, \quad 309.2 \pm 0.3\,. \qquad (6.5)$$

Note that the relative errors in the two larger variances are roughly the same ($\sim$ 0.1 %), while for the smallest variance is four times larger. This is a consequence

of the experimental setup: the smallest variance is directly revealed only in one of the recorded projections used for the reconstruction.

6.3 Discussion

In summary, we have presented a complete programme for the full polarization tomography of quantum states. Using the SU(2) Wigner function, we have provided an exact inversion formula in terms of the histograms of a standard Stokes measurement and derived a simplified version for very localized, high intensity states which turns out to be an inverse Radon transform. As a test of the theory, the reconstruction of an intense polarization squeezed state has been performed. A ML reconstruction algorithm has also been presented and has been compared to the direct method, thereby yielding an excellent agreement. Of course, the technique can be readily used for any other polarization state.

Chapter 7

Conclusions

In this thesis I have presented my research in the field of tomographic methods for various topics of modern optic. Both experimental and theoretical results are demonstrated and applications in quantum as well as classical optical signals are considered. After brief state of art survey describing the context of each presented application, particular tomography methods are discussed in detail.

In chapter 4, Shack-Hartmann wavefront sensor tomography is experimentally demonstrated. The possibility of characterization partially coherent optical fields with common wavefront sensor has been demonstrated. This goes further the standard analysis and constitutes a substantial leap ahead that might trigger potential applications in many areas. Applying quantum tomography to Shack-Hartmann data, the coherence matrix carrying complete information about the coherence properties and 3D intensity distribution of the signal can be reconstructed. This idea was illustrated with the experimental 3D imaging of optical vortices. To our best knowledge, this is the first experimental measurement of the coherence properties with a wavefront sensor. We emphasize that the standard Shack-Hartmann operation fails in this kind of application. The high-order vortex beams with strongly helical wavefronts are very difficult to analyze with the standard wavefront sensors, while they pose no difficulty for our proposed approach. Finally, reconstruction of coherence matrix from informationally incomplete measurement was carried out. Here, the Maximum Likelihood-Maximum entropy algorithm was performed and a good agreement with the results of informationally complete version of the measurement was obtained.

Chapter 5 is dedicated to data pattern tomography of photon distributions. The most relevant feature of the approach is the ability to perform an efficient reconstruction without ever knowing the exact properties of the measurement setup. The knowledge required for the precise estimation of a particular signal state can be obtained a posteriori, after the measurement on the signal state. This is a significant advantage for the experimentalists, since calibrating the measurement setups

can be a rather challenging task. Iterative procedure for obtaining information about the measurement which is sufficient for an estimation of a particular signal state was developed. The method can decide which probe states might be helpful in further improving of the reconstruction. The strategy was numerically verified by photon number distribution tomography of light pulses. We have explicitly demonstrated that coherent and thermal probe states provide adequate quantum resources for the reconstruction of highly non-classical states with few photons.

Finally, in chapter 6, tomography of bright squeezed light generated via the optical Kerr effect is described. Using Stokes measurements and high intensity states approximations, the tomographic reconstruction of the state is equivalent to an inverse Radon transformation of the measured Stokes tomograms. Reconstruction of the state Wigner function by direct inverse Radon transform was compared to results of a novel Maximum-Likelihood algorithm. For inverse Radon reconstruction, the complete set of 90^2 different measurements angles was used, whereas the maximum likelihood reconstruction only included 9^2 different measurement angles. The significantly greater statistical inversion stability of the maximum likelihood technique allows us to get reconstruction of the same quality but from far smaller data sets. This corresponds to a reduction of the measurement time by two orders of magnitude and hence allows for a much faster characterization of the polarization state. Furthermore, the artifacts present in the inverse Radon reconstruction are completely suppressed.

Curriculum vitae

- Name: Bohumil Stoklasa
- Date of Birth: November 24, 1984
- Education:

  2004-2007: BSc student of optics and optoelectronic, Faculty of Science, Palacky University Olomouc, received academic title BSc

  2007-2009: MSc student of optics and optoelectronic, Faculty of Science, Palacky University Olomouc, received title MSc

  2009- : PhD student of optics and optoelectronic, Faculty of Science, Palacky University Olomouc
- Working experience:

  From September 1, 2010 employed at the Dept. of Optics, Faculty of Science, Palacky University Olomouc as a junior researcher

  From September 1, 2009 employed at Meopta-Optika, s.r.o. as a measuring methods developer
- Scientific stays:

  January, 2012, February, 2013, November, 2013: Max-Planck Institute for Science of Light, Erlangen, Germany

  July-August, 2013: Universidad Complutense, Madrid, Spain
- Participation as a member in following research projects:

  2009-2012: project "Multispectral systems for visible and infrared spectral regions", No. FR-TI1/364 of Ministry of Industry and Trade of the Czech Republic

  2012- : project "Center of Digital Optics", No. TE01020229 of Ministry of Industry and Trade of the Czech Republic

2013-2014: project ”International Center for Information and Uncertainty” No. CZ. 1.07/2.3.00/20.0060 of the European Social Fund and Ministry of Education of the Czech Republic

- Achievements

  Winner of competition for young researches in physical science, ”Cena Milana Odehnala”, 2014

Publications of the author and citations list

- L. Motka, B. Stoklasa, J. Rehacek, Z. Hradil, V. Karasek, D. Mogilevtsev, G.Harder, C. Silberhorn, L. L. Sánchez-Soto, *Efficient algorithm for optimizing data-pattern tomography,* Phys. Rev. A. **89**, 054102 (2014)

- B. Stoklasa, L. Motka, J. Rehacek, Z. Hradil, L. L. Sánchez-Soto, *Wavefront sensing reveals optical coherence,* Nature Communications **5**, (2014)

- D. Mogilevtsev, A. Ignatenko, A. Maloshtan, B. Stoklasa, J. Rehacek, Z. Hradil, *Data pattern tomography: reconstruction with an unknown apparatus,* N. J. Phys. **14**, (2013)

- CH. Müller, B. Stoklasa, A. B. Klimov, Ch. Gabriel, Ch. Peuntinger, J. Rehacek, Z. Hradil, L. L. Sanchez-Soto, Ch. Marquardt, G. Leuchs, *Quantum polarization tomography of bright squeezed light,* N. J. Phys. **14**, (2012)

- B. Stoklasa, J. Rehacek, Z. Hradil, *Adaptive IR and VIS image fusion,* Proc. SPIE 8407, (2012)

- Y. S. Teo, B. Stoklasa, B.G. Englert, J. Rehacek, Z. Hradil, *Incomplete quantum state estimation: a comprehensive study,* Phys. Rev. A. **85**, 042317 (2012)

- D. Mogilevtsev, A. Ignatenko, A. Maloshtan, B. Stoklasa, J. Rehacek, Z. Hradil, *Data pattern tomography: reconstruction with an unknown apparatus,* N. J. Phys. **14**, (2013)

    1. Banaszek, K., Cramer, M., and Gross, D. (2013). Focus on quantum tomography. *New Journal of Physics*, 15(12):125020.
    2. Mogilevtsev, D., Hradil, Z., Rehacek, J., and Shchesnovich, V. (2013). Cross-validated tomography. *Physical review letters*, 111(12):120403.
    3. Cooper, M., Karpinski, M., and Smith, B. J. (2013). Quantum state estimation with unknown measurements. *arXiv preprint arXiv:1306.6431*.
    4. Song, H., Qi, B., and Xi, Z. (2013). On the quantum state estimation with imperfect observation. In *Control Conference (CCC), 2013 32nd Chinese*, pages 7929–7934. IEEE.

- CH. Müller, B. Stoklasa, A. B. Klimov, Ch. Gabriel, Ch. Peuntinger, J. Rehacek, Z. Hradil, L. L. Sanchez-Soto, Ch. Marquardt, G. Leuchs, *Quantum polarization tomography of bright squeezed light,* N. J. Phys. **14**, (2012)

    1. Goldschmidt, E. A., Piacentini, F., Berchera, I. R., Polyakov, S. V., Peters, S., Kück, S., Brida, G., Degiovanni, I. P., Migdall, A., and Genovese, M. (2013). Mode reconstruction of a light field by multiphoton statistics. *Physical Review A*, 88(1):013822.
    2. Klimov, A., Björk, G., and Sánchez-Soto, L. (2013). Optimal quantum tomography of permutationally invariant qubits. *Physical Review A*, 87(1):012109.
    3. Sánchez-Soto, L., Klimov, A., de la Hoz, P., and Leuchs, G. (2013). Quantum versus classical polarization states: when multipoles count. *arXiv preprint arXiv:1306.0351*.
    4. Rigas, I., Klimov, A., Sánchez-Soto, L., and Leuchs, G. (2013). Nonlinear cross-kerr quasiclassical dynamics. *New Journal of Physics*, 15(4):043038.
    5. Peuntinger, C., Heim, B., Müller, C. R., Gabriel, C., Marquardt, C., and Leuchs, G. (2014). Distribution of squeezed states through an atmospheric channel. *arXiv preprint arXiv:1402.6290*.
    6. de la Hoz, P., Klimov, A., Björk, G., Kim, Y.-H., Müller, C., Marquardt, C., Leuchs, G., and Sánchez-Soto, L. (2013). Multipolar hierarchy of efficient quantum polarization measures. *Physical Review A*, 88(6):063803.

7. Chekhova, M. and Khalili, F. Y. (2013). Nonclassical features of the polarization quasiprobability distribution. *Physical Review A*, 88(2):023822.
8. Klimov, A., Romero, J., and Wallentowitz, S. (2014). Quantum-state tomography for optical polarization with arbitrary photon numbers. *Physical Review A*, 89(2):020101.

■ Y. S. Teo, B. Stoklasa, B.G. Englert, J. Rehacek, Z. Hradil, *Incomplete quantum state estimation: a comprehensive study,* Phys. Rev. A. **85**, 042317 (2012)

1. Flammia, S. T., Gross, D., Liu, Y.-K., and Eisert, J. (2012). Quantum tomography via compressed sensing: error bounds, sample complexity and efficient estimators. *New Journal of Physics*, 14(9):095022.
2. Brańczyk, A., Mahler, D. H., Rozema, L. A., Darabi, A., Steinberg, A. M., and James, D. F. (2012). Self-calibrating quantum state tomography. *New Journal of Physics*, 14(8):085003.
3. Rosset, D., Ferretti-Schöbitz, R., Bancal, J.-D., Gisin, N., and Liang, Y.-C. (2012). Imperfect measurement settings: Implications for quantum state tomography and entanglement witnesses. *Physical Review A*, 86(6):062325.
4. Teo, Y. S., Englert, B.-G., Řeháček, J., and Hradil, Z. (2011). Adaptive schemes for incomplete quantum process tomography. *Physical Review A*, 84(6):062125.
5. Shang, J., Ng, H. K., Sehrawat, A., Li, X., and Englert, B.-G. (2013). Optimal error regions for quantum state estimation. *New Journal of Physics*, 15(12):123026.
6. Gonçalves, D., Lavor, C., Gomes-Ruggiero, M., Cesário, A., Vianna, R., and Maciel, T. (2013). Quantum state tomography with incomplete data: Maximum entropy and variational quantum tomography. *Physical Review A*, 87(5):052140.
7. Mohammadi, M., Brańczyk, A. M., and James, D. F. (2013). Fourier-transform quantum state tomography. *Physical Review A*, 87(1):012117.
8. Quesada, N., Brańczyk, A. M., and James, D. F. (2013). Self-calibrating tomography for multidimensional systems. *Physical Review A*, 87(6):062118.
9. Teo, Y. S., Englert, B.-G., Řeháček, J., Hradil, Z., and Mogilevtsev, D. (2012). Verification of state and entanglement with incomplete tomography. *New Journal of Physics*, 14(10):105020.

10. Qi, B., Hou, Z., Li, L., Dong, D., Xiang, G., and Guo, G. (2013). Quantum state tomography via linear regression estimation. *Scientific reports*, 3.

11. Teo, Y. S., Řeháček, J., and Hradil, Z. (2013b). Informationally incomplete quantum tomography. *Quantum Measurements and Quantum Metrology*, 1:57–83.

12. Riofrío, C. A. (2011). Continuous measurement quantum state tomography of atomic ensembles. *arXiv preprint arXiv:1111.5627*.

13. Teo, Y. S., Řeháček, J., and Hradil, Z. (2013a). Coarse-grained quantum state estimation for noisy measurements. *Physical Review A*, 88(2):022111.

14. Dai, J., Len, Y. L., Teo, Y. S., Englert, B.-G., and Krivitsky, L. A. (2014). Experimental detection of entanglement with optimal-witness families. *arXiv preprint arXiv:1402.5710*.

Stručné shrnutí v češtině

Práce "Tomografické metody v moderní optice" se zabývá několika technikami tomografických měření a tomografických protokolů v kvantové i klasické optice, zejména pak tomografií částečně koherentních optických svazků, tomografií polarizačního stavu neklasického světla a tomografií fotonových distribucí. Společný rámec všech pužitých metod je tvořen formalizmem kvantové tomografie.

V první části práce je popsán nejvýznamnější prezentovaný výsledek, vůbec první experimentální realizace detekce částečně koherentního optického pole pomocí Shack-Hartmannova detektoru, která byla provedena v laboratořích Univerzity Palackého. Tento experiment ukázal, že nová tomografická metoda zpracování dat tohoto široce používaného detektoru podstatně rozšiřuje jeho možnosti, konkrétně o detekci koherenční matice obsahující veškeré informace o světelném svazku. Tato vlastnost byla experimentálně demonstrována při predikci rozložení intenzity optického svazku v dalekém poli, kde uvedená metoda správně predikuje toto rozložení v konfrontaci z přímým měřením. V experimentu použité vírové optické svazky jsou velice zajímavou optickou strukturou pro optické mikromanipulace a přenos informace optickou cestou. Disertace dále obsahuje popis experimentu, kde je realizována Shack-Hartmannova tomografie s neúplnou sadou měření pro detekci Laguerre-Gauss svazků. Na tento problém byla aplikována metoda Maximum Likelihood-Maximum Entropy s velmi uspokojivými výsledky.

V následující kapitole je rozpracována aplikace tomografické metody "Data Patterns". Tato metoda řeší problém kalibrace měřícího aparátu a je tedy vhodná při komplikovaných měřeních s mnoha volnými parametry. Pro numerickou simulaci byla vybrána tomografie fotonových rozdělení při malém středním počtu fotonů, jako měřící zařízení pak Time-Multiplexing-Device. Práce obsahuje praktický numerický protokol výběru parametrů metody a prokazuje využitelnost techniky Data Patterns na problém neklasických stavů světla s malým středním počtem fotonů.

V poslední kapitole je popsán výsledek, který se podařilo dosáhnout společně s kolegy z Max-Planck Institute Erlangen, kde se experimentálně provádí měření neklasického stlačeného světla a jeho polarizačních vlastností. Námi aplikovaná metoda Maximum Likelihood na změřená tomografická data pomohla zkrátit dobu

měření z několika hodin na několik minut, což má velké důsledky pro stabilitu celého experimentu. Bylo třeba naprogramovat speciální software provádějící 3D rekonstrukci polarizační Wignerovy funkce, kde hlavním problémem bylo velké množství zpracovávaných dat.

Disertační práce se zakládá na čtyřech článcích z impaktovaných vědeckých časopisů, které jsem publikoval za spolupráce kolegů z katedry optiky UPOL, Max-Planck Institute Erlangen, Universidad Comlutense Madrid, Centre for Quantum Technologies Singapore a Institute of Physics Minsk. Jedná se o práce

B. Stoklasa, L. Motka, J. Rehacek, Z. Hradil, L. L. Sánchez-Soto, *Wavefront sensing reveals optical coherence,* Nature Communications **5**, (2014)

D. Mogilevtsev, A. Ignatenko, A. Maloshtan, B. Stoklasa, J. Rehacek, Z. Hradil, *Data pattern tomography: reconstruction with an unknown apparatus,* N. J. Phys. **14**, (2013)

CH. Müller, B. Stoklasa, A. B. Klimov, Ch. Gabriel, Ch. Peuntinger, J. Rehacek, Z. Hradil, L. L. Sanchez-Soto, Ch. Marquardt, G. Leuchs, *Quantum polarization tomography of bright squeezed light,* N. J. Phys. **14**, (2012)

Y. S. Teo, B. Stoklasa, B.G. Englert, J. Rehacek, Z. Hradil, *Incomplete quantum state estimation: a comprehensive study,* Phys. Rev. A. **85**, 042317 (2012)

Bibliography

[1] K. Vogel and H. Risken, Phys. Rev. A 40.5 (1989): 2847.

[2] D.T. Smithey, et al. , Phys. Rev. Lett. 70.9 (1993): 1244.

[3] U. Leonhardt, *Measuring the Quantum state of Light*, (Cambridge University Press, 1997).

[4] M. Paris and J. Řeháček, *Lecture Notes in Physics — Quantum State Estimation* (Springer, Berlin Heidelberg, 2004).

[5] M. Nielsen and L. Chuang, *Quantum computation and quantum information*, (Cambridge university press, 2010).

[6] U .L. Andersen, G. Leuchs, and Ch. Silberhorn, *Continuous variable quantum information processing*, Laser and Photonics Reviews 4.3 (2010): 337-354.

[7] R. Schack, T. A. Brun, and C. M. Caves, PRA**64**, 014305 (2001).

[8] R. Blume-Kohout and P. Hayden, eprint arXiv:0603116 [quant-ph] (2006).

[9] R. Blume-Kohout, New J. Phys. **12**, 043034 (2010).

[10] R. A. Fisher, Phil. Trans. R. Soc. London **A 222**, 309 (1922).

[11] C. W. Helstrøm, *Quantum Detection and Estimation Theory*, Academic Press, New York (1976).

[12] J. Řeháček, Z. Hradil, E. Knill, and A. I. Lvovsky, PRA **75**, 042108 (2007).

[13] Y. S. Teo, H. Zhu, B.-G. Englert, J. Řeháček, and Z. Hradil, PRL **107**, 020404 (2011).

[14] D. N. Klyshko, Sov. J. Quantum Electron. **10**, 1112 (1980).

[15] A. A. Malygin, A. N. Penin, A. V. Sergienko, Sov. Phys. JETP Lett. **33**, 477 (1981).

[16] G. M. D'Ariano, L. Maccone, and P. LoPresti, Phys. Rev. Lett. **93**, 250407 (2004)

[17] G. Brida, M. Genovese, M. Gramegna, Las. Phys. Lett.**3**, 115 (2006).

[18] S.V. Polyakov and A.L. Migdall, Opt. Express **15**, 1390 (2007).

[19] D. Mogilevtsev, Phys. Rev. A **82**, 021807(R) (2010).

[20] Z. Hradil, D. Mogilevtsev, and J. Rehacek, New J. Phys. **10**, 043022 (2008).

[21] J. S. Lundeen, A. Feito, H. Coldenstrodt-Ronge, K. L. Pregnell, Ch. Silberhorn, T. C. Ralph, J. Eisert, M. B. Plenio and I. A. Walmsley, Nature Physics **5**, 27 (2009).

[22] J. Rehacek, S. Olivares, D. Mogilevtsev, Z. Hradil, M. G. A. Paris, S. Fornaro, V. D'Auria, A. Porzio, and S. Solimeno, Phys. Rev. A **79**, 032111 (2009).

[23] M. Mohseni and D. A. Lidar, Phys. Rev. Lett. **97** 170501 (2006); *ibid* Phys. Rev. A **75**, 062331 (2007); M. Mohseni, A. T. Rezakhani and D. A. Lidar, Phys. Rev. A **77** 032322 (2008).

[24] C. T. Schmiegelow, M. A. Larotonda, and J. P. Paz, Phys. Rev. Lett. **104**, 123601 (2010); C. T. Schmiegelow, A. Bendersky, M. A. Larotonda, and J. P. Paz, Phys. Rev. Lett. **107**, 100502 (2011).

[25] D. Malacara, ed., *Optical Shop Testing* (Wiley, Hoboken, 2007), 3rd ed.

[26] G.-M. Dai, *Wavefront Optics for Vision Correction* (SPIE Press, Bellingham, 2008).

[27] J. Ares, T. Mancebo, and S. BarÂ·, Appl. Opt. **39**, 1511–1520 (2000).

[28] O. Katz, E. Small, Y. Bromberg, and Y. Silberberg, Nat. Photon. **5**, 372–377 (2011).

[29] D. J. McCabe, A. Tajalli, D. R. Austin, P. Bondareff, I. A. Walmsley, S. Gigan, and B. Chatel, Nat. Commun. **2**, 447 (2011).

[30] A. P. Mosk, A. Lagendijk, G. Lerosey, and M. Fink, Nat. Photon. **6**, 283–292 (2012).

[31] R. K. Tyson, *Principles of Adaptive Optics* (CRC Press, Boca Raton, 2011), 3rd ed.

[32] J. M. Geary, *Introduction to Wavefront Sensors* (SPIE Press, Bellingham, 1995).

[33] D. R. Luke, J. V. Burke, and R. G. Lyon, SIAM Rev. **44**, 169—224 (2002).

[34] H. I. Campbell and A. H. Greenaway, "Wavefront sensing: From historical roots to the state-of-the-art." EAS Publications **22**, 165–185 (2006).

[35] B. C. Platt and R. S. Shack, "History and principles of Shack-Hartmann wavefront sensing," J. Refract. Surg. **17**, S573–S577 (2001).

[36] J. Primot, Opt. Commun. **222**, 81–92 (2003).

[37] L. Mandel and E. Wolf, *Optical Coherence and Quantum Optics* (Cambridge University Press, Cambridge, 1995).

[38] Z. Hradil, J. Řeháček, and L. L. Sánchez-Soto, Phys. Rev. Lett. **105**, 010401 (2010).

[39] Muller A, Breguet J and Gisin N, Europhys. Lett. **23** 383–388 (1993)

[40] Mattle K, Weinfurter H, Kwiat P G and Zeilinger A, Phys. Rev. Lett. **76** 4656–4659 (1996)

[41] Bouwmeester D, Pan J W, Mattle K, Eibl M, Weinfurter H and Zeilinger A, Nature **390** 575–579 (1997)

[42] Rådmark M, Żukowski M and Bourennane M, New J. Phys. **11** 103016 (2009)

[43] Resch K J, Pregnell K L, Prevedel R, Gilchrist A, Pryde G J, O'Brien J L and White A G, Phys. Rev. Lett. **98** 223601 (2007)

[44] Dixon P B, Starling D J, Jordan A N and Howell J C, Phys. Rev. Lett. **102** 173601 (2009)

[45] Lamas-Linares A, Howell J C and Bouwmeester D, Nature **412** 887–890 (2001)

[46] Sehat A, Söderholm J, Björk G, Espinoza P, Klimov A B and Sánchez-Soto L L, Phys. Rev. A **71** 033818 (2005)

[47] White A G, James D F V, Eberhard P H and Kwiat P G, Phys. Rev. Lett. **83** 3103–3107 (1999)

[48] Kwiat P G, Berglund A J, Altepeter J B and White A G, Science **290** 498–501 (2000)

[49] James D F V, Kwiat P G, Munro W J and White A G, Phys. Rev. A **64** 052312 (2001)

[50] Thew R T, Nemoto K, White A G and Munro W J, Phys. Rev. A **66** 012303 (2002)

[51] Barbieri M, De Martini F, Di Nepi G, Mataloni P, D'Ariano G M and Macchiavello C, Phys. Rev. Lett. **91** 227901 (2003)

[52] Bogdanov Y I, Chekhova M V, Kulik S P, Maslennikov G A, Zhukov A A, Oh C H and Tey M K, Phys. Rev. Lett. **93** 230503 (2004)

[53] Moreva E V, Maslennikov G A, Straupe S S and Kulik S P, Phys. Rev. Lett. **97** 023602 (2006)

[54] Barbieri M, Vallone G, Mataloni P and De Martini F, Phys. Rev. A **75** 042317 (2007)

[55] Adamson R B A and Steinberg A M, Phys. Rev. Lett. **105** 030406 (2010)

[56] Sansoni L, Sciarrino F, Vallone G, Mataloni P, Crespi A, Ramponi R and Osellame R, Phys. Rev. Lett. **105** 200503 (2010)

[57] Altepeter J B, Oza N N, Medi M, Jeffrey E R and Kumar P, Opt. Express **19** 26011–26016 (2011)

[58] Chirkin A S, Orlov A A and Parashchuk D Y, Quantum Electron. **23** 870–874 (1993)

[59] Korolkova N, Leuchs G, Loudon R, Ralph T C and Silberhorn C, Phys. Rev. A **65** 052306 (2002)

[60] Luis A and Korolkova N, Phys. Rev. A **74** 043817 (2006)

[61] Mahler D, Joanis P, Vilim R and de Guise H, New J. Phys. **12** 033037 (2010)

[62] Bowen W P, Schnabel R, Bachor H A and Lam P K, Phys. Rev. Lett. **88** 093601 (2002)

[63] Heersink J, Gaber T, Lorenz S, Glöckl O, Korolkova N and Leuchs G, Phys. Rev. A **68** 013815 (2003)

[64] Dong R, Heersink J, Yoshikawa J I, Glöckl O, Andersen U L and Leuchs G, New J. Phys. **9** 410 (2007)

[65] Shalm L K, A A R B and Steinberg A M, Nature **457** 67–70 (2009)

[66] Iskhakov T, Chekhova M V and Leuchs G, Phys. Rev. Lett. **102** 183602 (2009)

[67] Brosseau C *Fundamentals of Polarized Light: A Statistical Optics Approach* (New York: Wiley) (1998)

[68] Raymer M G and Funk A C, Phys. Rev. A **61** 015801 (1999)

[69] Raymer M G, McAlister D F and Funk A, Measuring the quantum polarization state of light *Quantum Communication, Computing, and Measurement 2* ed Kumar P (New York: Plenum) (2000)

[70] Karassiov V P, J. Phys. A **26** 4345–4354 (1993)

[71] Bushev P A, Karassiov V P, Masalov A V and Putilin A A, Opt. Spectrosc. **91** 526–531 (2001)

[72] Karassiov V P and Masalov A V, JETP **99** 51–60 (2004)

[73] Karassiov V, J. Russ. Las. Res. **26** 484–513 (2005)

[74] Marquardt C, Heersink J, Dong R, Chekhova M V, Klimov A B, Sánchez-Soto L L, Andersen U L and Leuchs G, Phys. Rev. Lett. **99** 220401 (2007)

[75] E. T. Jaynes, Phys. Rev. **106**, 620 (1957), Phys. Rev. **108**, 171 (1957).

[76] V. Bužek, G. Adam, and G. Drobny, Ann. Phys. (N.Y.) **245**, 37 (1996).

[77] A. R. Rossi and M.G.A. Paris, Eur. Phys. J. D **32**, 223 (2005).

[78] Y. S. Teo, H. Zhu, B.-G. Englert, J. Řeháček, and Z. Hradil, PRL **107**, 020404 (2011).

[79] J. Rehacek, D. Mogilevtsev, and Z. Hradil, Phys Rev Lett. **105**, 010402(2010).

[80] R. G. Gonzalez and R. E. Woods, *Digital Image Processing* (Prentice-Hall, Englewood Cliffs, NJ, 2002), 2nd ed.

[81] J. W. Goodman, *Introduction to Fourier Optics* (Roberts, Greenwood Village, 2005), 3rd ed.

[82] E. Arthurs and J. L. J. Kelly, Bell Syst. Tech. J. **44**, 725–729 (1965).

[83] S. Stenholm, Ann. Phys. **218**, 197–198 (1992).

[84] M. G. Raymer, Am. J. Phys. **62**, 986–993 (1994).

[85] K. Husimi, Proc. Phys. Math. Soc. Jpn. **22**, 264–314 (1940).

[86] A. I. Lvovsky and M. G. Raymer, Rev. Mod. Phys. **81**, 299–322 (2009).

[87] P. Busch and P. Lahti, Found. Phys. **19**, 633–678 (1989).

[88] U. Leonhardt and M. Munroe, Phys. Rev. A **54**, 3682–3684 (1996).

[89] D. Sych, J. Řeháček, Z. Hradil, G. Leuchs, and L. L. Sánchez-Soto, Phys. Rev. A **86**, 052123 (2012).

[90] Hradil Z, Mogilevtsev D and Řeháček J, Phys. Rev. Lett. **96** 230401 (2006)

[91] Stratonovich R L, JETP **31** 1012—1020 (1956)

[92] Berezin F A, Commun. Math. Phys. **40** 153–174 (1975)

[93] Agarwal G S, Phys. Rev. A **24** 2889–2896 (1981)

[94] Brif C and Mann A, J. Phys. A **31** L9–L17 (1998)

[95] Varilly J C and Gracia-Bondía J M, Ann. Phys. **190** 107–148 (1989)

[96] Heiss S and Weigert S, Phys. Rev. A **63** 012105 (2000)

[97] Klimov A B and Chumakov S M, J. Opt. Soc. Am. A **17** 2315–2318 (2000)

[98] Klimov A B and Romero J L, J. Phys. A **41** 055303 (2008)

[99] Heersink J, Josse V, Leuchs G and Andersen U L, Opt. Lett. **30** 1192–1194 (2005)

[100] Karassiov V P, JETP Lett. **84** 640–644 (2006)

[101] Karassiov V P and Kulik S P, JETP **104** 30—46 (2007)

[102] Schwinger J, On angular momentum *Quantum Theory of Angular Momentum* ed Biedenharn L C and Dam H (New York: Academic) (1965)

[103] Chaturvedi S, Marmo G and Mukunda N, Rev. Math. Phys. **18** 887–912 (2006)

[104] Luis A and Sánchez-Soto L L, Prog. Opt. **41** 421–481 (2000)

[105] Born M and Wolf E, Principles of Optics 7th ed (Cambridge: Cambridge University Press) (1999)

[106] Corney J F, Heersink J, Dong R, Josse V, Drummond P D, Leuchs G and Andersen U L, Phys. Rev. A **78** 023831 (2008)

[107] Grangier P, Slusher R E, Yurke B and LaPorta A, Phys. Rev. Lett. **59** 2153–2156 (1987)

[108] Smithey D T, Beck M, Raymer M G and Faridani A, Phys. Rev. Lett. **70** 1244–1247 (1993)

[109] Schnabel R, Bowen W P, Treps N, Ralph T C, Bachor H A and Lam P K, Phys. Rev. A **67** 012316 (2003)

[110] Julsgaard B, Sherson J, Cirac J I, Fiurasek J and Polzik E S, Nature **432** 482–486 (2004)

[111] Josse V, Dantan A, Bramati A and Giacobino E, J. Opt. B **6** S532–S543 (2004)

[112] Dowling J P, Agarwal G S and Schleich W P, Phys. Rev. A **49** 4101–4109 (1994)

[113] Atakishiyev N M, Chumakov S M and Wolf K B, J. Math. Phys. **39** 6247–6261 (1998)

[114] Chumakov S M, Frank A and Wolf K B, Phys. Rev. A **60** 1817–1822 (1999)

[115] Chumakov S M, Klimov A B and Wolf K B, Phys. Rev. A **61** 034101 (2000)

[116] Klimov A B, J. Math. Phys. **43** 2202–2213 (2002)

[117] Varshalovich D A, Moskalev A N and Khersonskii V K, Quantum Theory of Angular Momentum (Singapore: World Scientific) (1988)

[118] Blum K, Density Matrix Theory and Applications (New York: Plenum) (1981)

[119] Klimov A B and Chumakov S M, J. Opt. Soc. Am. A **17** 2315–2318 (2000)

[120] Brif C and Mann A, Phys. Rev. A **59** 971–987 (1999)

[121] Amiet J P and Weigert S, J. Phys. A **32** L269–L274 (1999)

[122] D'Ariano G M, Maccone L and Paini M, J. Opt. B **5** 77–84 (2003)

[123] Klimov A B, Man'ko O V, Man'ko V I, Smirnov Y F and Tolstoy V N, J. Phys. A **35** 6101–6123 (2002)

[124] D. Achilles, C. Silberhorn, C. Śliwa, K. Banaszek, and I. A. Walmsley, Opt. Lett. 28, 2387 (2003); O. Haderka, M. Hamar, and J. Peřina, Eur. Phys. J. D **28**, 149 (2004).

[125] J. Řeháček, Z. Hradil, O. Haderka, J. Peřina, Jr., and M. Hamar, PRA **67**, 061801(R) (2003).

[126] S. Wallentowitz and W. Vogel, PRA **53**, 4528 (1996).

[127] G. Molina-Terriza, J. P. Torres, and L. Torner, Nat. Phys. **3**, 305–310 (2007).

[128] J. Torres and L. Torner, eds., *Twisted Photons: Applications of Light with Orbital Angular Momentum.* (Wiley-VCH, Weinheim, 2011).

[129] Z. Hradil, D. Mogilevtsev, and J. Řeháček, Phys. Rev. Lett. **96**, 230401 (2006).

[130] J. Řeháček, Z. Hradil, Z. Bouchal, R. Čelechovský, I. Rigas, and L. L. Sánchez-Soto, Phys. Rev. Lett. **103**, 250402 (2009).

[131] H. Cramér, *Mathematical Methods of Statistics* (Princeton University, Princeton, 1946).

[132] C. R. Rao, *Linear Statistical Inference and Its Applications* (Wiley, New York, 1973).

[133] Y. I. Bogdanov, G. Brida, I. D. Bukeev, M. Genovese, K. S. Kravtsov, S. P. Kulik, E. V. Moreva, A. A. Soloviev, and A. P. Shurupov, Phys. Rev. A **84**, 042108 (2011).

[134] J. W. Goodman, *Introduction to Fourier Optics* (Roberts, Greenwood Village, 2005), 3rd ed.

[135] M. R. Teague, J. Opt. Soc. Am. A **73**, 1434–1441 (1983).

[136] F. Roddier, Appl. Opt. **29**, 1402–1403 (1990).

[137] B. Schäfer and K. Mann, Appl. Opt. **41**, 2809–2817 (2002).

[138] A. Mair, A. Vaziri, G. Weihs, and A. Zeilinger, Nature **412**, 313 (2001).

[139] D. M. Appleby, Int. J. Theor. Phys. **37**, 1491–1509 (1998).

[140] G. Hinshaw, J. L. Weiland, R. S. Hill, N. Odegard, D. Larson, C. L. Bennett, J. Dunkley, B. Gold, M. R. Greason, N. Jarosik, E. Komatsu, M. R. Nolta, L. Page, D. N. Spergel, E. Wollack, M. Halpern, A. Kogut, M. Limon, S. S. Meyer, G. S. Tucker, and E. L. Wright, Astrophys. J. Suppl Ser. **180**, 225–245 (2009).

[141] R. C. Cannon, J. Opt. Soc. Am. A **12**, 2031–2039 (1995).

[142] H. H. Barrett, C. Dainty, and D. Lara, J. Opt. Soc. Am. A **24**, 391–414 (2007).

[143] R. G. Gonzalez and R. E. Woods, *Digital Image Processing* (Prentice-Hall, Englewood Cliffs, NJ, 2002), 2nd ed.

[144] R. J. Glauber, Phys. Rev. Lett. **10**, 84 (1963).

[145] E. C. G. Sudarshan, Phys. Rev. Lett. **10** 277 (1963).

[146] J. R. Klauder, Phys. Rev. Lett. **16**, 534 (1966).

[147] M. Lobino, D. Korystov, C. Kupchak, E. Figueroa, B. C. Sanders and A. I. Lvovsky, Science **322**, 563 (2008); S. Rahimi-Keshari, A. Scherer, A. Mann, A. T. Rezakhani, A. I. Lvovsky and B. C Sanders, New J. Phys. **13**, 013006 (2011).

[148] J. F. Corney and P. D. Drummond, Phys. Rev. A **68**, 063822 (2003).

[149] V. A. Vilnrotter and C.-W. Lau, IPN Progress Report **42**, 152(2003).

[150] D. Mogilevtsev, Opt. Comm. **156**, 307 (1998); D. Mogilevtsev, Acta Physica Slovaca **49**, 743 (1999).

[151] A.R. Rossi, S. Olivares, M.G.A. Paris, Phys. Rev. A **70**, 055801 (2004); A.R. Rossi and M.G.A. Paris, Eur. Phys. J. D **32**, 223 (2005); G. Zambra, A. Andreoni, M. Bondani, M. Gramegna, M. Genovese, G. Brida, A. Rossi, and M.G.A. Paris, Phys. Rev. Lett. **95** 063602 (2005).

[152] Z. Hradil, D. Mogilevtsev, and J. Rehacek, Phys. Rev. Lett. **96**, 230401 (2006); D. Mogilevtsev, J. Rehacek and Z. Hradil, Phys. Rev. A **75**, 012112 (2007).

[153] J. Rehacek, Z. Hradil, O. Haderka, J. Perina Jr, M. Hamar, Phys. Rev. A **67**, 061801(R) (2003); O. Haderka, M. Hamar, J. Perina Jr, Eur. Phys. J. D **28**, 149 (2004).

[154] J. G. Webb and E. H. Huntington, Opt. Exp. **17** 11799 (2009).

[155] Shelby R M, Levenson M D and Bayer P W, Phys. Rev. B **31** 5244–5252 (1985)

[156] Shelby R M, Levenson M D, Perlmutter S H, DeVoe R G and Walls D F, Phys. Rev. Lett. **57** 691–694 (1986)

[157] Elser D, Andersen U L, Korn A, Glöckl O, Lorenz S, Marquardt C and Leuchs G, Phys. Rev. Lett. **97** 133901 (2006)

[158] Thode H C, *Testing for Normality* (New York: Marcel Dekker) (2002)

[159] Paris M G A and Řeháček J (eds) , *Quantum State Estimation* (*Lect. Not. Phys.* vol 649) (Berlin: Springer) (2004)

[160] Dempster A P, Laird N M and Rubin D B, J. R. Statist. Soc. B **39** 1–38 (1977)

[161] Boyles R A, J. R. Statist. Soc. B **45** 47–50 (1983)

[162] Vardi Y and Lee D, J. R. Statist. Soc. B **55** 569–612 (1993)

[163] Řeháček J, Olivares S, Mogilevtsev D, Hradil Z, Paris M G A, Fornaro S, D'Auria V, Porzio A and Solimeno S, Phys. Rev. A **79** 032111 (2009)

1. Název práce: Tomografické metody v moderní optice

2. Název v angličtině: Tomographic methods in modern optics

3. Souběžný název:

4. Anotace:
   V disertační práci jsou popsány aplikace kvantové tomografie v moderní optice. Obsahem jsou jak experimentální výsledky, tak rozpracování tomografických algoritmů. V prvním případě se jedná jednak o tomografii koherenční funkce světelných svazků s využitím detekce vlnoplochy a jednak o tomografii stlačeného polarizačního stavu světla. V druhém případě je popsán tomografický algoritmus "Data patterns" na příkladu tomografie fotonového rozdělení optických pulsů. Algoritmus MLME pro informačně nekompletní měření je prezentován i experimentálně a je aplikován na tomografie vlnoplochy.

5. Klíčová slova: kvantová tomografie, tomografické algoritmy, polarizace světla, koherence světla, detekce vlnoplochy, fotonové distribuce

6. Anotace v angličtině:
   In the thesis, different applications of quantum tomography are presented. Both experimental results and tomographic protocols are discussed. Experimental part includes a coherence function tomography of light beams using wavefront detection and polarization squeezed light tomography. Tomographic protocols involved "Data pattern" approach illustrated a by photon distribution tomography. Protocol MLME for informationally incomplete measurement is also experimentally applicated to wavefront tomography.

7. Anglická klíčová slova: quantum tomography, tomographic algorithms, polarization of light, coherence of light, wavefront detection, photon number distribution

8. Přílohy:

9. Přílohy vázané v práci:

10. Rozsah práce: i-iii, 1-82

11. Jazyk práce: Angličtina